

Photonic and QCD radiative corrections to
Higgs-boson production in $\mu^+\mu^- \rightarrow f\bar{f}$

STEFAN DITTMAYER^{1†} AND ANDREAS KAISER²

¹ *Deutsches Elektronen-Synchrotron DESY
D-22603 Hamburg, Germany*

² *Paul Scherrer Institut
CH-5232 Villigen PSI, Switzerland*

Abstract:

The photonic and QCD radiative corrections at next-to-leading order are calculated for fermion-pair production at muon colliders, maintaining the full mass dependence and helicity information of the muons and the produced fermions. Higher-order effects of initial-state radiation are included at the leading logarithmic level. In the calculation particular attention is paid to the issue of gauge invariance in the vicinity of resonances. The most important corrections are presented in analytical form. The detailed numerical discussion concentrates on the corrections to the (s -channel) Higgs-boson resonances in the Standard Model and its minimal supersymmetric extension. The results show that photonic initial- and QCD final-state corrections are very important in a precision study of Higgs resonances, but that (photonic) initial-final interferences are widely suppressed and only modify the non-resonant background.

March 2002

[†]Heisenberg fellow of the Deutsche Forschungsgemeinschaft

1 Introduction

The search for Higgs bosons will be among the most prominent ambitions in future high-energy collider experiments. Once one or even more Higgs bosons are found at the Tevatron [1], the LHC [2], or a future e^+e^- collider [3], it is necessary to determine the properties of these particles, such as their masses, decay widths, and couplings, in order to reconstruct the scalar sector of the underlying spontaneously broken gauge theory. Current electroweak precision data [4] and the direct search for a Higgs boson at LEP2 [5] constrain the mass M_H of the Standard Model (SM) Higgs boson to $M_H < 222$ GeV and $M_H > 114$ GeV at the 95% C.L., respectively. In the Minimal Supersymmetric extensions of the SM (MSSM) the lower bound for the light Higgs boson h is about $M_h > 91$ GeV [6], while an upper bound of $M_h \lesssim 130$ GeV results from theoretical constraints (see e.g. Refs. [7, 8] and references therein). Thus, it seems very promising to search for a Higgs boson with mass $\lesssim 140$ GeV. Since the decay channel into on-shell W and Z bosons is not yet open in this mass range, such a Higgs boson has a very narrow width, rendering its *direct* measurement in a resonance distribution impossible at hadron and e^+e^- colliders.

A muon collider provides the unique opportunity to investigate Higgs-boson resonances in the s -channel within the clean environment of a lepton collider, since the Yukawa coupling of Higgs bosons to the initial-state muons is about 200 times larger than for e^\pm , resulting in a relative enhancement by a factor 40000. Studies [9] of the experimental feasibility of a muon collider show that the beam energy resolution can even be small enough to resolve a Higgs resonance with a width of some MeV, as it for instance appears for a SM-like Higgs boson with mass $\lesssim 140$ GeV. To be specific, for a SM Higgs boson of $M_H \sim 110$ GeV the relative accuracies achievable by scanning the $\mu^+\mu^- \rightarrow H \rightarrow b\bar{b}$ resonance with a luminosity of 0.2 fb^{-1} was estimated in Refs. [10, 11, 12] to be $\sim 1 - 3 \times 10^{-6}$ and 0.2 for the mass and total width, respectively. Moreover, observing the reaction $\mu^+\mu^- \rightarrow H \rightarrow f\bar{f}$, is complementary to Higgs production at e^+e^- machines where the Higgs boson is produced via its couplings to Z or W bosons. The high accuracy at a muon collider also allows for a better discrimination between a SM and a SM-like Higgs boson in extended models like the MSSM as compared to hadron or e^+e^- colliders. Furthermore, the existence of a SM-like Higgs boson h in the MSSM means that the two other MSSM Higgs bosons A and H are heavy; in this case a muon collider also proves to be the most promising machine to study the properties of these Higgs bosons. For instance, measuring the mass difference $M_H - M_A$ yields an important check of the Higgs mass relations [7, 8] in the MSSM, as pointed out in Ref. [13]. More information on the Higgs phenomenology at muon colliders can be found in the literature [9, 10, 11, 12, 13, 14, 15, 16, 17] including in particular studies of CP violation [14], Higgs decays into $\tau^+\tau^-$ pairs [15], and flavour-changing neutral currents [16]. In this context, the possibility to produce polarized muon beams proved to be very useful.

In this paper we calculate the photonic and QCD corrections to the fermion-pair production processes $\mu^+\mu^- \rightarrow f\bar{f}$ in the SM and the MSSM. These corrections represent an important ingredient in a precision calculation of the Higgs resonances in these channels. In particular, photonic initial-state radiation (ISR) distorts the resonance shape, as it is, e.g., well known from studies of the Z resonance in e^+e^- annihilation (see e.g. Ref. [18] and references therein). In contrast to the e^+e^- case, however, we have to include the

finite-mass effects of both initial-state and final-state fermions, since Higgs production proceeds via the so-called spin-0 channel which is mass suppressed. In detail, we calculate the full photonic $\mathcal{O}(\alpha)$ correction, which decomposes into ISR, final-state radiation (FSR) and initial-final interferences, and include the leading ISR effects beyond $\mathcal{O}(\alpha)$ in the structure-function approach [19]. In some existing studies ISR effects were already included at the leading logarithmic level as described in the appendix of Ref. [11]; however, non-leading corrections have not yet been presented elsewhere. These effects are of particular importance if polarized muon beams are considered, since the leading logarithmic approach ignores a possible spin flip of radiating muons, which mixes the spin-0 and spin-1 channels. QCD corrections are evaluated in next-to-leading order, i.e. in $\mathcal{O}(\alpha_s)$, also taking into account the full mass dependence. For b quarks in the final state the running $\overline{\text{MS}}$ mass is introduced.

In our discussion of numerical results we mainly focus on $b\bar{b}$ final states and consider SM Higgs-boson resonances for $M_H = 115 \text{ GeV}$ and 150 GeV . In the MSSM we discuss two interesting scenarios, one where the H/A resonances lie on top of each other and one where they are sufficiently separated in mass. In the latter case, the masses are chosen large enough to enable an inclusion of $t\bar{t}$ production. Cross sections for polarized muons are only briefly discussed, although our calculation fully supports helicity eigenstates¹ of the external fermions.

The non-photonic, i.e. purely weak, electroweak radiative corrections of $\mathcal{O}(G_\mu)$ are not considered in this paper for the following reasons. It is known (see e.g. Ref. [18]) that photonic corrections, in particular ISR effects, comprise a very important gauge-invariant class of radiative corrections to resonance processes of neutral particles. Another important source of corrections are renormalization effects, such as the running of the electromagnetic coupling α . The latter universal effect is included by appropriately choosing the input value of α . Moreover, a fully convincing calculation of the non-photonic $\mathcal{O}(G_\mu)$ corrections is intrinsically connected to the Dyson summation of all relevant propagator corrections without losing gauge invariance. We discuss this issue in detail for the photonic and QCD corrections and give an outlook to the non-photonic corrections, where the problem is more involved. In summary, our results can be viewed as a first step towards a precision calculation, and the weak corrections are part in one of the next steps. If one is only interested in a precise prediction of the Higgs resonance shapes, a reasonable approach would be to include the weak corrections to the Higgs Yukawa couplings on the Higgs resonances in the framework of effective couplings. This procedure maintains gauge invariance and the effective couplings can be easily combined with the photonic and QCD corrections discussed here. The most important weak corrections to the Higgs Yukawa couplings in the MSSM have already been discussed in Ref. [20].

The paper is organized as follows: In Section 2 we set our conventions and calculate the lowest-order cross sections. Section 3 contains our discussion of gauge invariance. The photonic corrections are treated in Section 4, where our explicit analytical results for the ISR and FSR effects can be found. The QCD corrections are deduced from the photonic FSR results in Section 5. Section 6 provides a detailed discussion of numerical results for

¹The generalization to other polarization states, such as transversely polarized beams, is straightforward.

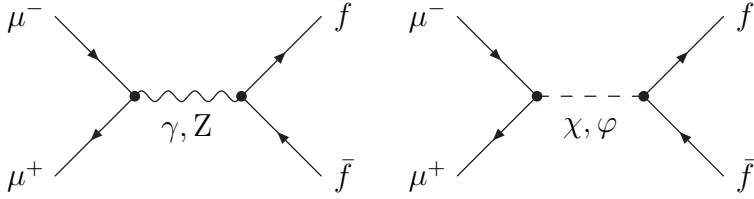


Figure 1: Lowest-order diagrams for $\mu^- \mu^+ \rightarrow f \bar{f}$ with $f \neq \mu^-$

the various corrections near the Higgs resonances. Our conclusions are given in Section 7, and the Appendix provides some auxiliary formulas.

2 Notation and lowest-order cross sections

We consider the process

$$\mu^-(p, \sigma) + \mu^+(p', \sigma') \longrightarrow f(q, \tau) + \bar{f}(q', \tau'), \quad f \neq \mu^-, \quad (2.1)$$

where the momenta p, \dots and helicities σ, \dots of the muons and fermions f are given in parentheses. The helicities take the values $\sigma = \pm \frac{1}{2}$, etc., but we will also take their sign to indicate the helicity. In lowest order the diagrams of Figure 1 contribute to the process (2.1). In order to treat the SM and MSSM in one go, we have abbreviated the Higgs bosons by φ , where $\varphi = H$ in the SM and $\varphi = h, H, A$ in the MSSM. The field χ denotes the would-be Goldstone partner of the Z boson; in the unitary gauge the diagram involving χ exchange is absent.

In the following we denote the vector and axial-vector couplings of the neutral gauge bosons to the fermions by

$$v_{\gamma f} = -Q_f, \quad a_{\gamma f} = 0, \quad v_{Zf} = \frac{s_w}{c_w} Q_f - \frac{I_{w,f}}{2c_w s_w}, \quad a_{Zf} = -\frac{I_{w,f}}{2c_w s_w}, \quad (2.2)$$

where $I_{w,f} = \pm \frac{1}{2}$ is the weak isospin of the left-handed part of the fermion field f , and Q_f is its electric charge. The corresponding Feynman rule for the $V_\mu f \bar{f}$ vertex is given by $ie\gamma_\mu(v_{Vf} - a_{Vf}\gamma_5)$, where e is the electric unit charge. In these couplings the parameters s_w and c_w are functions of the weak mixing angle θ_w ,

$$\sin^2 \theta_w = s_w^2 = 1 - c_w^2, \quad c_w = \frac{M_W}{M_Z}, \quad (2.3)$$

and thus fixed by the ratio of the gauge-boson masses M_W and M_Z . For the vertices $Sf\bar{f}$ and $Pf\bar{f}$ of fermions with the neutral scalar and pseudo-scalar fields S and P we generically write the Feynman rules as ieg_{Sf} and $eg_{Pf}\gamma_5$, respectively. For the pseudo-scalar would-be Goldstone field χ the coupling factor reads

$$g_{\chi f} = -\frac{I_{w,f}}{s_w c_w} \frac{m_f}{\hat{M}_Z}, \quad (2.4)$$

where m_f is the mass of the fermion f . Here we write \hat{M}_Z for the Z-boson mass instead of M_Z for later convenience; the definition of \hat{M}_Z and its relation to M_Z will be discussed

in Section 3 in detail. While the $\chi f \bar{f}$ coupling is equal in the SM and the MSSM, the couplings of the fermions to the Higgs bosons, of course, differ in these models. We follow the conventions of Ref. [21] also for the SM and define

$$\begin{aligned}
\text{SM:} \quad & g_{\text{H}f} = -\frac{1}{2c_w s_w} \frac{m_f}{M_Z}, \\
\text{MSSM:} \quad & g_{\text{h}u} = -\frac{1}{2c_w s_w} \frac{m_u \cos \alpha}{M_Z \sin \beta}, \quad g_{\text{h}d} = +\frac{1}{2c_w s_w} \frac{m_d \sin \alpha}{M_Z \cos \beta}, \\
& g_{\text{H}u} = -\frac{1}{2c_w s_w} \frac{m_u \sin \alpha}{M_Z \sin \beta}, \quad g_{\text{H}d} = -\frac{1}{2c_w s_w} \frac{m_d \cos \alpha}{M_Z \cos \beta}, \\
& g_{\text{A}u} = -\frac{1}{2c_w s_w} \frac{m_u}{M_Z} \cot \beta, \quad g_{\text{A}d} = -\frac{1}{2c_w s_w} \frac{m_d}{M_Z} \tan \beta, \quad (2.5)
\end{aligned}$$

where u and d refer to up- and down-type fermions, respectively. In the SM the Yukawa coupling $eg_{\text{H}f}$ is entirely determined by the ratio m_f/v , where $v = 1/\sqrt{\sqrt{2}G_\mu}$ is the vacuum expectation value of the Higgs field. In the MSSM the couplings additionally depend on the angles α and β , which are related to the masses of the Higgs bosons. We follow the usual convention to use the mass M_A and $\tan \beta = v_2/v_1$ as independent input parameters, where $v_{1,2}$ are the vacuum expectation values of the two Higgs doublets in the MSSM. The angle α as well as the other Higgs masses M_h and M_H are then derived from M_A , $\tan \beta$, and the parameters of the gauge sector; to this end we employ the program *HDECAY* [22] which calculates α , the dependent Higgs masses, and the Higgs decay widths Γ_φ , thereby including also some leading radiative corrections [7] to these relations.

Sometimes it is more convenient to decompose the fermionic couplings into their right- and left-handed parts, which are proportional to the chirality projectors $\omega_\pm = (1 \pm \gamma_5)/2$, instead of using vector, axial-vector, scalar, and pseudo-scalar couplings. Therefore, we introduce the right- and left-handed coupling factors g_{\dots}^\pm for the various couplings introduced above,

$$g_{\text{V}f}^\pm = v_{\text{V}f} \mp a_{\text{V}f}, \quad g_{\text{S}f}^\pm = g_{\text{S}f}, \quad g_{\text{P}f}^\pm = \mp i g_{\text{P}f}, \quad (2.6)$$

so that the Feynman rule for the $V_\mu f \bar{f}$ vertex is given by $ie\gamma_\mu(g_{\text{V}f}^+\omega_+ + g_{\text{V}f}^-\omega_-)$ and the rules for the scalar or pseudo-scalar field $\varphi = \text{S, P}$ generically read $ie(g_{\varphi f}^+\omega_+ + g_{\varphi f}^-\omega_-)$.

The Mandelstam variables for the process (2.1) are defined as usual,

$$s = (p + p')^2, \quad t = (p - q)^2, \quad u = (p - q')^2. \quad (2.7)$$

In the calculation of the tree-level amplitude \mathcal{M}_0 and of the one-loop amplitude \mathcal{M}_1 , which is described in the next section, we separate the fermion spinor chains by defining the following standard matrix elements (SME),

$$\begin{aligned}
\mathcal{M}_1^{\{v,a\}\{v,a\}} &= [\bar{v}_{\mu+} \gamma_\rho \{1, \gamma_5\} u_{\mu-}] [\bar{u}_f \gamma^\rho \{1, \gamma_5\} v_{\bar{f}}], \\
\mathcal{M}_2^{\{v,a\}\{v,a\}} &= [\bar{v}_{\mu+} \{1, \gamma_5\} u_{\mu-}] [\bar{u}_f \{1, \gamma_5\} v_{\bar{f}}], \\
\mathcal{M}_3^{\{v,a\}\{v,a\}} &= [\bar{v}_{\mu+} \not{d} \{1, \gamma_5\} u_{\mu-}] [\bar{u}_f \{1, \gamma_5\} v_{\bar{f}}], \\
\mathcal{M}_4^{\{v,a\}\{v,a\}} &= [\bar{v}_{\mu+} \{1, \gamma_5\} u_{\mu-}] [\bar{u}_f \not{d} \{1, \gamma_5\} v_{\bar{f}}], \quad (2.8)
\end{aligned}$$

with an obvious notation for the Dirac spinors \bar{v}_{μ^+} , etc. The labels v and a in the SME refer to the insertions of 1 or γ_5 in the two spinor chains; for instance we have $\mathcal{M}_2^{va} = [\bar{v}_{\mu^+} u_{\mu^-}][\bar{u}_f \gamma_5 v_f]$. The explicit expressions of the SME for all possible helicity configurations can be found in the Appendix. The SME represent 16 independent functions which form a basis for the tree-level and one-loop amplitudes, i.e. these amplitudes admit the representation

$$\mathcal{M}_n = \sum_{i=1}^4 \sum_{x,y=v,a} F_{n,i}^{xy}(s,t) \mathcal{M}_i^{xy}, \quad n = 0, 1, \quad (2.9)$$

with Lorentz invariant functions $F_{n,i}^{xy}(s,t)$. The lowest-order amplitude reads

$$\mathcal{M}_0 = \sum_{V=\gamma,Z} \mathcal{M}_{V,0} + \sum_{P=\chi,A} \mathcal{M}_{P,0} + \sum_{S=h,H} \mathcal{M}_{S,0} \quad (2.10)$$

with

$$\begin{aligned} \mathcal{M}_{V,0} &= \frac{e^2}{s - \hat{M}_V^2} (v_{V\mu} v_{Vf} \mathcal{M}_1^{vv} - v_{V\mu} a_{Vf} \mathcal{M}_1^{va} - a_{V\mu} v_{Vf} \mathcal{M}_1^{av} + a_{V\mu} a_{Vf} \mathcal{M}_1^{aa}), \\ \mathcal{M}_{P,0} &= \frac{e^2 g_{P\mu} g_{Pf}}{s - \hat{M}_P^2} \mathcal{M}_2^{aa}, \\ \mathcal{M}_{S,0} &= -\frac{e^2 g_{S\mu} g_{Sf}}{s - \hat{M}_S^2} \mathcal{M}_2^{vv}, \end{aligned} \quad (2.11)$$

where it is understood that the sums over P and S extend only over χ and H, respectively, in the case of the SM. In a pure lowest-order prediction the propagator denominators $(s - M^2)$ lead to infinities in the resonance point $s = M^2$. A perturbative description of these resonances requires a Dyson summation of propagator corrections that regularize the unphysical divergence. Here we signal the propagator modification, which is explained in the next section in detail, by putting carets over the masses in the propagators. For the photon we, of course, have $\hat{M}_\gamma = 0$.

Ignoring the Dyson summation for the moment, in Eq. (2.10) the contribution of $P = \chi$ results from the sum of χ exchange and of the $k_\mu k_\nu$ part of Z-boson propagator in a general R_ξ gauge, with k denoting the transferred momentum. The unitary gauge and the 't Hooft–Feynman gauge represent two interesting special cases. In the unitary gauge the χ diagram is absent and the $P = \chi$ part is completely due to the $k_\mu k_\nu$ part of the Z propagator; in the 't Hooft–Feynman it is the other way round.

Finally, the lowest-order cross section reads

$$\sigma_0 = \frac{N_{c,f} \beta_f}{64\pi^2 s \beta_\mu} \int d\Omega_f \sum_{\sigma,\sigma',\tau,\tau'} \frac{1}{4} (1 + 2P_- \sigma)(1 + 2P_+ \sigma') |\mathcal{M}_0(\sigma, \sigma', \tau, \tau')|^2, \quad (2.12)$$

where

$$\beta_\mu = \sqrt{1 - \frac{4m_\mu^2}{s}}, \quad \beta_f = \sqrt{1 - \frac{4m_f^2}{s}}, \quad (2.13)$$

are the velocities of the muons and produced fermions in the centre-of-mass (CM) frame, where also the solid angle Ω_f of f is defined, and $N_{c,f}$ is the number of colours of f , which is 1 if f is a lepton and 3 if f is a quark. The degrees of polarization in the μ^\pm beams are denoted by P_\pm and range from -1 to $+1$.

3 The issue of gauge invariance

3.1 Preliminaries

We first consider the case of a single resonance appearing in a propagator with momentum transfer k and (renormalized) mass M . In lowest order the resonance appears for $k^2 \rightarrow M^2$ where the lowest-order propagator has a pole, and a proper description of the resonance requires a Dyson summation of the self-energy corrections to the resonant propagator. After this summation, in the vicinity of the resonance the amplitude \mathcal{M} behaves as

$$\mathcal{M} \sim \frac{R}{k^2 - M^2 + \Sigma(k^2)} + \text{non-resonant terms}, \quad (3.1)$$

where $\Sigma(k^2)$ denotes the self-energy of the propagating particle. The resonance appears for a value of k^2 where $k^2 - M^2 + \text{Re}\{\Sigma(k^2)\} = 0$. Since $\Sigma(k^2)$ develops a non-vanishing imaginary part in this resonance region, the propagator pole is shifted away from the real axis into the complex k^2 plane. We denote the complex location of this pole by $\bar{M}^2 - i\bar{M}\bar{\Gamma}$ in the following. The real quantities \bar{M} and $\bar{\Gamma}$ provide a consistent definition of the particle's mass and width, respectively. In particular, for gauge theories it was shown [23] that this definition is related to the bare parameters of the theory in a gauge-invariant way. Making use of \bar{M} and $\bar{\Gamma}$, the naive propagator modification

$$\frac{1}{k^2 - M^2} \rightarrow \frac{1}{k^2 - \bar{M}^2 + i\bar{M}\bar{\Gamma}}, \quad (3.2)$$

which is known as *fixed-width scheme*, yields a possible description of the resonance in lowest order.

Another definition of the particle's mass is provided by the zero of the real part of the resonance denominator in Eq. (3.1), known as *on-shell definition*, which we identify with M in the following. This definition was, for instance, adopted for the Z-boson mass at LEP1. The quantities M and \bar{M} coincide up to one-loop order, but differ at two loops and beyond. Making use of the usual renormalization conditions in the on-shell scheme, $\text{Re}\{\Sigma(M^2)\} = 0$ and $\text{Re}\{\Sigma'(M^2)\} = 0$, the resonance behaviour of the propagator in Eq. (3.1) is obtained from the lowest order by the substitution

$$\frac{1}{k^2 - M^2} \rightarrow \frac{1}{k^2 - M^2 + iM\Gamma(k^2)}. \quad (3.3)$$

In the approximation of massless decay products the running width $\Gamma(k^2)$ is related to the on-shell decay width Γ by $\Gamma(k^2) = \Gamma \times k^2/M^2 \theta(k^2)$. The parametrization (3.3) is known as *running-width scheme*. It can be checked easily that the parameter sets $(\bar{M}, \bar{\Gamma})$ and (M, Γ) , when extracted upon fitting the parametrizations (3.2) and (3.3) to data, are related by [24]

$$\begin{aligned} \bar{M} &= M/\sqrt{1 + \gamma^2} = M - \frac{\Gamma^2}{2M} + \dots, & \gamma &= \Gamma/M, \\ \bar{\Gamma} &= \Gamma/\sqrt{1 + \gamma^2} = \Gamma - \frac{\Gamma^3}{2M^2} + \dots, \\ \bar{R} &= R/(1 + i\gamma) = R \left(1 - i\frac{\Gamma}{M} + \dots \right), \end{aligned} \quad (3.4)$$

where we have also included the relation of the corresponding residues \bar{R} and R .

At first sight it seems that the naive propagator modifications (3.2) and (3.3) yield reasonable descriptions of the resonance at least in lowest order. However, this is not the case in general, since this modification potentially violates the gauge-invariance properties of the full amplitude. Gauge invariance implies relations between self-energy, vertex, and box corrections (etc.) that in particular guarantee the cancellation of gauge-fixing parameters within the amplitude. These generalized Ward identities work order by order in perturbation theory, i.e. they are jeopardized by any kind of partial inclusion of higher-order corrections, such as the modification (3.2) which resums part of the self-energy corrections. Therefore, finite decay widths have to be introduced very carefully, in particular if radiative corrections are taken into account, which additionally complicate the situation.

3.2 Survey of photonic and QCD corrections — gauge-invariant subsets of Feynman graphs

Before we explicitly describe our treatment of the resonances occurring in the process (2.1), it is useful to identify gauge-invariant subsets of Feynman graphs within the inspected class of corrections.

At tree level (see Figure 1) only Z-boson and χ exchange diagrams are linked by gauge invariance, while each diagram with photon or Higgs-boson exchange is gauge invariant in itself. This is also reflected by the fact that the Z- and Higgs-boson masses in the propagators can be viewed as independent parameters in the lowest-order diagrams. While this argument is trivially correct in the SM, where M_H is a free parameter, it works in the MSSM since the same diagrams appear, for instance, in a general two-Higgs-doublet model, where the masses are completely unrelated. Thus, the MSSM relations among the Higgs masses do not disturb this gauge-invariance property of the (tree-level) diagrams.

Next we consider the photonic $\mathcal{O}(\alpha)$ corrections, which are induced by one-loop photon exchange diagrams and real emission of a single photon. This subclass of electroweak corrections is gauge-invariant, since a consistent $U(1)_{\text{elmg}}$ gauge theory of the neutral bosons (γ , Z, and Higgs bosons) and all other fermions is conceivable, in which the process (2.1) proceeds in the same way as in the SM or MSSM in lowest order. If W bosons were involved at tree level this would be not the case. The photonic one-loop and bremsstrahlung diagrams that are relevant in $\mathcal{O}(\alpha)$ are collected in Figures 2–4; the corresponding counterterm graphs are not shown explicitly. Of course, virtual and real corrections are separately gauge-invariant, since they correspond to different final states. However, these corrections are connected in the domains of soft and collinear photon emission, and these relations between one-loop diagrams and their real counterparts have to be preserved in the introduction of finite decay widths. Otherwise IR divergences and/or collinear singularities in the high-energy limit might not cancel properly. Therefore, we do not separate virtual and real corrections in the following discussion.

Using the same argument as for the tree-level graphs, the diagrams of the photonic corrections can be further divided into gauge-invariant subsets according to the boson that is exchanged in the related tree-level graph. Thus, we have a gauge-invariant subset with internal photons only, one with Z-boson or χ exchange, and one for each type of Higgs bosons. Furthermore, each of these subsets splits into three gauge-invariant parts

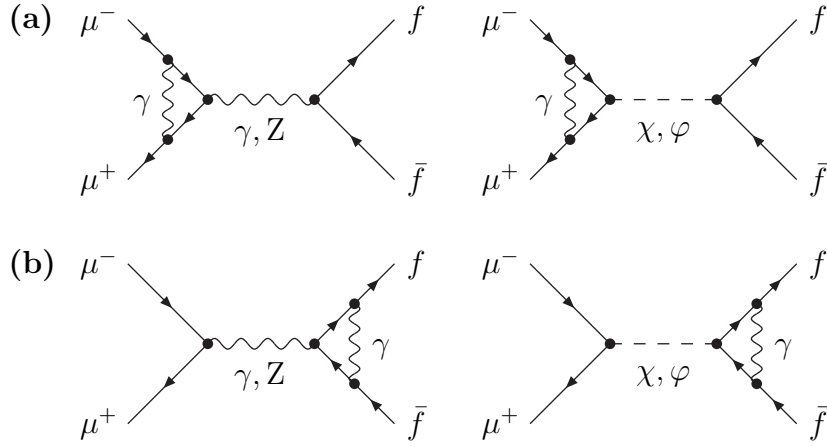


Figure 2: Diagrams for photonic vertex corrections to $\mu^-\mu^+ \rightarrow f\bar{f}$ contributing to (a) initial-state and (b) final-state corrections with φ denoting any Higgs boson

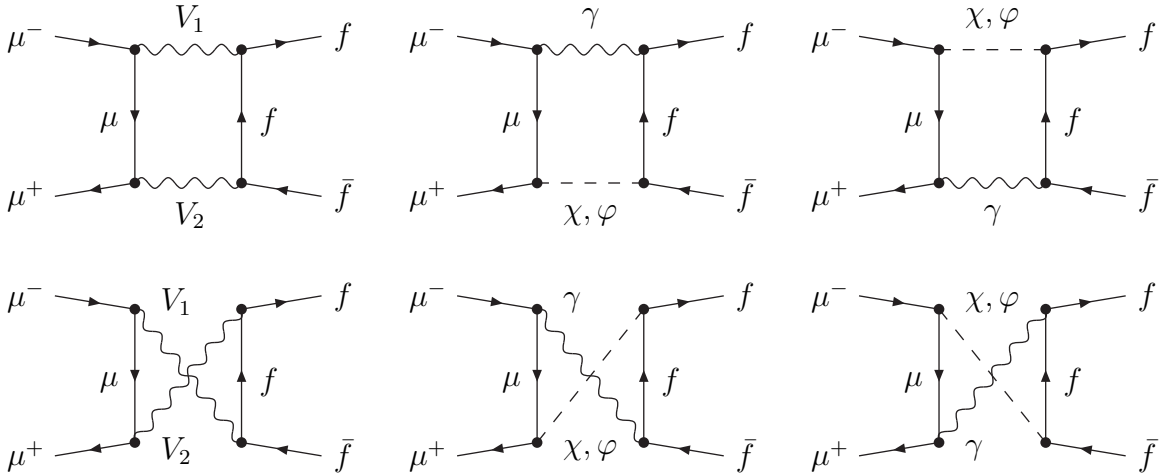


Figure 3: Photonic box diagrams for $\mu^-\mu^+ \rightarrow f\bar{f}$ with $V_1V_2 = \gamma\gamma, \gamma Z, Z\gamma$ and φ denoting any Higgs boson

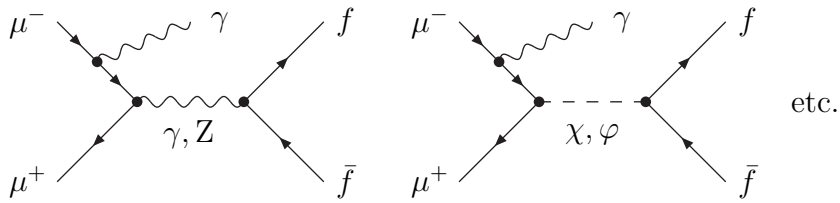


Figure 4: Lowest-order diagrams for $\mu^-\mu^+ \rightarrow f\bar{f}\gamma$ with φ denoting any Higgs boson. Graphs with the outgoing photon attached to the fermions f, \bar{f} are not shown.

according to the charge factors of the two fermions to which the exchanged or emitted photon is attached. In this way we distinguish initial-state corrections, final-state corrections, and corrections connecting initial and final state. The relative correction factors are proportional to Q_μ^2 , Q_f^2 , and $Q_\mu Q_f$, respectively. The corresponding one-loop diagrams are shown in Figures 2(a), 2(b), and 3, respectively; the related squared diagrams of real photon emission should be clear.

The $\mathcal{O}(\alpha_s)$ QCD corrections, which are only present if the fermion f is a quark, are closely related to the photonic final-state corrections of $\mathcal{O}(\alpha)$. The QCD diagrams are obtained from the photon exchange or emission diagrams upon replacing the loop-exchanged or emitted photon by a gluon. The QCD diagrams are, thus, classified exactly in the same way as the photonic final-state corrections.

3.3 Treatment of Z-boson and Higgs resonances

In the following we describe a simple way of introducing finite widths for the Z and Higgs bosons in the process (2.1) that retains gauge invariance in the presence of photonic and QCD corrections.

As explained in the previous section, each Higgs-boson mass can be viewed as an independent parameter as long as we inspect only photonic and QCD corrections. Thus, a possible way of introducing finite Higgs-boson widths is provided by substituting the real Higgs masses squared by the complex pole positions in all Higgs propagators. Since all relations induced by gauge invariance, such as the cancellation of the gauge-parameter dependence in the photon propagator, are of algebraic nature, they are not destroyed by this substitution. For Higgs bosons the difference between barred and unbarred mass and width parameters will not be experimentally significant, so that there is no need to distinguish between barred and unbarred quantities any further. Thus, for the Higgs masses appearing in Eq. (2.10) we set

$$\hat{M}_\varphi^2 = M_\varphi^2 - iM_\varphi\Gamma_\varphi, \quad \varphi = h, H, A. \quad (3.5)$$

For Z-boson and χ exchange the situation is much more involved, since the poles in the longitudinal part of the Z-boson propagator and the one in the χ propagator are unphysical and have to cancel each other properly. We perform this cancellation explicitly in a general R_ξ gauge, where the free propagators are given by

$$\begin{aligned} G_{\mu\nu}^{ZZ}(k) &= \frac{-i}{k^2 - M_Z^2 + iM_Z\Gamma_Z(k^2)} \left(g_{\mu\nu} - \frac{k_\mu k_\nu}{k^2} \right) - \frac{i\xi_Z}{k^2 - \xi_Z M_Z^2} \frac{k_\mu k_\nu}{k^2}, \\ G^{\chi\chi}(k) &= \frac{i}{k^2 - \xi_Z M_Z^2}, \end{aligned} \quad (3.6)$$

with ξ_Z denoting the gauge-fixing parameter of the Z field. Here we have already taken into account that the transverse part of the Z propagator receives a contribution of the physical gauge-boson width after Dyson summation, while the longitudinal part and the χ propagator do not. The actual form of the function $\Gamma_Z(k^2)$ for the width is left open for the moment.² In the diagrams for the tree level, for the one-loop, and for the bremsstrahlung

²Contributions that do not change the resonance structure, such as real parts of self-energies or γZ mixing effects, are not included in the Dyson summation, since they are part of the purely weak correction not considered in this paper.

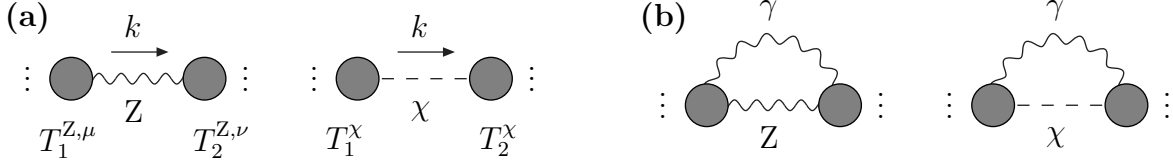


Figure 5: Subdiagrams with Z and χ exchange. The blobs represent tree-like or loop parts, and the dots stand for external (on-shell) fermion or photon fields.

corrections, shown in Figures 1–4, the propagators (3.6) appear in the two different ways schematically shown in Figure 5. The subdiagrams (a) contain Z or χ fields on a tree-like line, i.e. cutting this line the diagram is decomposed into two disconnected parts; the subdiagrams (b) contain a Z or χ line within a loop. As indicated in Figure 5, we denote the structures of the blobs in subdiagrams (a) by $T_n^{Z,\mu}$ and T_n^χ ($n = 1, 2$). The functions T are nothing but (photonic parts of) amputated Green functions for off-shell Z or χ fields contracted with the wave functions for the remaining external fields of μ^+ , μ^- , f , \bar{f} , or γ which are all on shell. Since subdiagrams (a) form a subset of gauge-invariant diagrams (see previous section), the T functions obey the same well-known Ward identities (see e.g. Refs. [25, 26]³) as the full amputated Green functions that are on-shell contracted for all legs other than the Z or χ line:

$$-k_\mu T_1^{Z,\mu}(-k) = -iM_Z T_1^\chi(-k), \quad k_\nu T_2^{Z,\nu}(k) = -iM_Z T_2^\chi(k), \quad (3.7)$$

where $\mp k$ in the argument of $T_{1,2}$ are the incoming momenta of the subdiagrams. Using these identities the contribution $\mathcal{M}_{(a)}$ of class (a) takes the form

$$\begin{aligned} \mathcal{M}_{(a)} &= T_1^{Z,\mu}(-k) G_{\mu\nu}^{ZZ}(k) T_2^{Z,\nu}(k) + T_1^\chi(-k) G^{\chi\chi}(k) T_2^\chi(k) \\ &= \frac{-iT_1^{Z,\mu}(-k) T_{2,\mu}^Z(k)}{k^2 - M_Z^2 + iM_Z \Gamma_Z(k^2)} + \frac{iT_1^\chi(-k) T_2^\chi(k) [k^2 + iM_Z \Gamma_Z(k^2)]}{k^2 [k^2 - M_Z^2 + iM_Z \Gamma_Z(k^2)]}, \end{aligned} \quad (3.8)$$

where the arbitrary gauge parameter ξ_Z has dropped out, as it should be. For diagrams of class (b) we proceed similarly. An important difference is, however, that the subdiagrams contained in the blobs do not obey Ward identities like Eq. (3.7) separately, because the blobs are linked. Instead the whole rest of the diagram without the Z or χ line can be viewed as part of an amputated Green function with external on-shell particles μ^+ , μ^- , f , \bar{f} and two off-shell Z or χ legs. These parts of Green functions, denoted by $T^{ZZ,\mu\nu}(-k, k)$ and $T^{\chi\chi}(-k, k)$, obey the Ward identity

$$k_\mu k_\nu T^{ZZ,\mu\nu}(-k, k) = M_Z^2 T^{\chi\chi}(-k, k), \quad (3.9)$$

as we have also checked explicitly for the box diagrams. Maybe it is interesting to note that really the sum of all four relevant box diagrams on both sides of Eq. (3.9) is needed for the identity, i.e. it is not valid for the pairs of box diagrams obtained by interchanging Z and χ lines. The contribution $\mathcal{M}_{(b)}$ of class (b) can, thus, be written as

$$\mathcal{M}_{(b)} = \int \frac{d^4 k}{(2\pi)^4} \left\{ T^{ZZ,\mu\nu}(-k, k) G_{\mu\nu}^{ZZ}(k) + T^{\chi\chi}(-k, k) G^{\chi\chi}(k) \right\}$$

³Note that there is a global sign difference in the Ward identity in Ref. [26] because of the different sign convention in the $SU(2)$ gauge coupling e/s_w .

$$= \int \frac{d^4k}{(2\pi)^4} \left\{ \frac{-iT_\mu^{ZZ,\mu}(-k, k)}{k^2 - M_Z^2 + iM_Z\Gamma_Z(k^2)} + \frac{iT^{\chi\chi}(-k, k) [k^2 + iM_Z\Gamma_Z(k^2)]}{k^2 [k^2 - M_Z^2 + iM_Z\Gamma_Z(k^2)]} \right\}, \quad (3.10)$$

where the loop integration has been made explicit.

Now we have to specify how to choose the function $\Gamma_Z(k^2)$ describing the Z-boson width. It is interesting to note that the simple choice of identifying $\Gamma_Z(k^2)$ with the (on-shell) width Γ_Z is not consistent, although $\Gamma_Z(M_Z^2) = \Gamma_Z$ on resonance. The reason for this failure is an artificial infrared (IR) divergence in the loop integral of $\mathcal{M}_{(b)}$, which appears in the second term in the curly bracket of Eq. (3.10) for $k^2 \rightarrow 0$. The divergence is, however, avoided if the k^2 dependence of $\Gamma_Z(k^2)$ is taken into account, since $\Gamma_Z(k^2 \rightarrow 0) = 0$. We, therefore, set $\Gamma_Z(k^2) = \Gamma_Z \times k^2/M_Z^2$ which is exact for massless decay products and $k^2 > 0$. The case $k^2 < 0$, where $\Gamma_Z(k^2)$ actually vanishes, only occurs in the box loop integrals $\mathcal{M}_{(b)}$, and the effect that we do not set $\Gamma_Z(k^2)$ to zero there is of the order $\alpha\Gamma_Z/M_Z$, i.e. beyond our accuracy. The benefit of the chosen form for $\Gamma_Z(k^2)$ becomes obvious after inserting $\Gamma_Z(k^2)$ and reparametrizing $\mathcal{M}_{(a)}$ and $\mathcal{M}_{(b)}$ by the complex-pole parameters \bar{M}_Z and $\bar{\Gamma}_Z$:

$$\begin{aligned} \mathcal{M}_{(a)} &= (1 + i\gamma_Z)^{-1} \left\{ \frac{-iT_1^{Z,\mu}(-k)T_{2,\mu}^Z(k) + i\bar{T}_1^\chi(-k)\bar{T}_2^\chi(k)}{k^2 - \bar{M}_Z^2 + i\bar{M}_Z\bar{\Gamma}_Z} \right\}, \\ \mathcal{M}_{(b)} &= (1 + i\gamma_Z)^{-1} \int \frac{d^4k}{(2\pi)^4} \left\{ \frac{-iT_\mu^{ZZ,\mu}(-k, k) + i\bar{T}^{\chi\chi}(-k, k)}{k^2 - \bar{M}_Z^2 + i\bar{M}_Z\bar{\Gamma}_Z} \right\}, \end{aligned} \quad (3.11)$$

where we have defined $\gamma_Z = \Gamma_Z/M_Z$ and

$$\bar{T}_n^\chi(k) = \sqrt{1 + i\gamma_Z} T_n^\chi(k), \quad \bar{T}^{\chi\chi}(-k, k) = (1 + i\gamma_Z) T^{\chi\chi}(-k, k), \quad n = 1, 2. \quad (3.12)$$

The rescaling (3.12) is equivalent to substituting $M_Z^2 \rightarrow \bar{M}_Z^2 - i\bar{M}_Z\bar{\Gamma}_Z$ in T_n^χ and $T^{\chi\chi}$, since these functions are proportional to M_Z^{-1} and M_Z^{-2} , respectively, because of the coupling (2.4) of the χ field to fermions.

In summary, we have shown that the consistent use of the propagators (3.6), where only the imaginary part, $M_Z\Gamma_Z(k^2)$, of the transverse Z-boson self-energy is Dyson summed, together with the approximation $\Gamma_Z(k^2) = \Gamma_Z \times k^2/M_Z^2$ is equivalent to an overall replacement $M_Z \rightarrow \sqrt{\bar{M}_Z^2 - i\bar{M}_Z\bar{\Gamma}_Z}$ in all graphs with Z-boson or χ exchange before any Dyson summation is done, up to the global scaling factor $(1 + i\gamma_Z)^{-1}$. This observation again shows that no (algebraic) relations induced by gauge invariance are violated in this procedure. In our following calculation we make consistent use of the form (3.11), but drop the global scaling factor $(1 + i\gamma_Z)^{-1}$, since it influences squared amplitudes only at the level Γ_Z^2/M_Z^2 or $\Gamma_Z\Gamma_\varphi/(M_Z M_\varphi)$, which is beyond the accuracy of interest. This means that we set

$$\hat{M}_Z^2 = \hat{M}_\chi^2 = \bar{M}_Z^2 - i\bar{M}_Z\bar{\Gamma}_Z \quad (3.13)$$

in Eqs. (2.4) and (2.11).

3.4 Outlook

We emphasize that the procedure described in the previous section cannot be taken over without modifications to include the genuine weak $\mathcal{O}(\alpha)$ corrections (also denoted

by $\mathcal{O}(G_\mu)$ elsewhere) where the situation is more involved. The main complication is due to the fact that weak self-energy, vertex, and box corrections are all gauge-dependent and connected by gauge invariance. These relations have to be preserved by the Dyson summation. One possibility to introduce finite decay widths in the resonance propagators without losing gauge invariance is provided by the *pole scheme* [28], where each propagator is expanded about its resonance pole and only the part of the residue, which is gauge-invariant, gets a finite width in the denominator. Details of the actual application of this scheme can also be found in Ref. [29], where it was applied to the Higgs resonance in $ZZ \rightarrow ZZ$, including electroweak $\mathcal{O}(\alpha)$ corrections. In the pole expansions, of course, care has to be taken that the relations between photonic virtual and real corrections in the soft and collinear regions are still retained, which might additionally complicate the application.

The discussion of the previous section raises the question about a possibility to consistently use complex mass values, which are derived from the complex locations $\bar{M}^2 - i\bar{M}\bar{\Gamma}$ of the propagator poles, as renormalized mass parameters. If the complex masses for the W and Z bosons are used in the definition (2.3) of the weak mixing angle, all generalized Ward identities, and thus gauge invariance, remains valid. This *complex-mass scheme* has been introduced in Ref. [30] for lowest-order predictions. However, whether this scheme is also consistent for the treatment of radiative corrections is not yet clear, since the use of complex mass and coupling parameters is field-theoretically questionable.

The field theoretically most desirable solution certainly consists in a consistent Dyson summation of all propagators (in fixed-order predictions), since this includes effects of running couplings directly in the propagator denominators. While this procedure in general violates gauge invariance in the conventionally quantized gauge theory, as explained also above, it was shown [26] that gauge invariance is preserved after Dyson summation within the background-field formalism [27]. However, following this approach in a consistent one-loop calculation, the finite widths introduced via Dyson-summed one-loop self-energies are tree-level quantities, i.e. the prediction obtained this way is not yet fully $\mathcal{O}(\alpha)$ -corrected. Although it is not yet clear whether or how this problem can be solved consistently in a pragmatic way, the background-field approach seems to be very promising.

The above considerations apply to a full inclusion of all weak $\mathcal{O}(\alpha)$ corrections both to resonant and non-resonant contributions. If one is only interested in a precise prediction of the Higgs resonance shapes, a simpler procedure is feasible. A reasonable approach would be to include the weak corrections to the Higgs Yukawa couplings in terms of effective couplings, i.e. the coupling parameters (2.5) would be dressed by the weak radiative corrections to the (on-shell) $\varphi f \bar{f}$ vertices, and to treat the photonic and QCD corrections as described in this paper. This is possible for the following reasons. Firstly, it is known (see also the numerical results below) that the interference of the Higgs bosons with the continuous background is totally negligible, since the former results from the spin-0 and the latter from the spin-1 channel. Secondly, there is no problem with gauge invariance, because each set of Higgs-exchange diagrams is gauge-invariant at tree level and in the presence of photonic and QCD corrections, as explained above.

4 Photonic radiative corrections

4.1 Virtual photonic corrections

The virtual one-loop corrections add coherently to the lowest-order matrix element \mathcal{M}_0 given in Eq. (2.10). Denoting the one-loop contribution to \mathcal{M}_0 that is induced by photon exchange by $\mathcal{M}_1^{(\gamma)}$, the one-loop-corrected squared matrix element reads

$$|\mathcal{M}|^2 = |\mathcal{M}_0|^2 + 2 \operatorname{Re}\{\mathcal{M}_1^{(\gamma)} \mathcal{M}_0^*\} + \dots, \quad (4.1)$$

where the dots stand for the genuine weak corrections of $\mathcal{O}(G_\mu)$, not considered in this paper, and higher-order terms. The one-loop correction σ_1 to the cross section is obtained by replacing $|\mathcal{M}_0|^2$ in Eq. (2.12) by the one-loop contribution of $|\mathcal{M}|^2$. As explained in the previous section, the one-loop correction $\mathcal{M}_1^{(\gamma)}$ receives contributions from vertex and box corrections,

$$\mathcal{M}_1^{(\gamma)} = \mathcal{M}_{\text{vert}}^{(\gamma)} + \mathcal{M}_{\text{box}}^{(\gamma)}, \quad (4.2)$$

which will be considered in the next two subsections in detail.

The actual calculation of the one-loop diagrams has been carried out using standard techniques. The Feynman graphs have been generated with *FeynArts* [31] and are evaluated in two independent ways. In the first calculation *FeynCalc* [32] is used to express the amplitudes in terms of SME and to reduce the occurring tensor integrals algebraically to scalar integrals with the Passarino–Veltman algorithm [33]. In the second calculation, also performed with *Mathematica* but without *FeynCalc*, we express the amplitudes in terms of SME and tensor coefficients. The reduction of the latter to scalar integrals is then done numerically. The results of the two calculations are in perfect numerical agreement (i.e. within machine accuracy for non-exceptional phase-space points). In both calculations the scalar integrals are evaluated using the methods and results of Refs. [34, 35, 36], where ultraviolet divergences are regulated dimensionally and IR divergences with infinitesimal photon and gluon masses, m_γ and m_g , respectively. The renormalization is carried out in the on-shell renormalization scheme, as e.g. described in Ref. [36].

4.1.1 Vertex corrections

In the on-shell renormalization scheme the external self-energy corrections are exactly cancelled by counterterms. Thus, the virtual vertex corrections induced by photon exchange are entirely given by the diagrams shown in Figure 2 and the counterterm contribution for the vertices. Among the relevant renormalization constants, only the one for the masses, δm_μ and δm_f , and for the fields, δZ^μ and δZ^f , receive photonic corrections, which can be easily derived from the general results given in Ref. [36]. We immediately give results for the renormalized vertices.

The vertex functions for the fermionic couplings of a general vector boson V, of a pseudo-scalar boson P, and of a scalar boson S are parametrized by

$$\begin{aligned} \Gamma_\rho^{\text{V}f}(q, q') &= ie\gamma_\rho(v_{\text{V}f} - a_{\text{V}f}\gamma_5) \\ &+ ieQ_f^2 \frac{\alpha}{4\pi} \left[\gamma_\rho(v_{\text{V}f} - a_{\text{V}f}\gamma_5)\Lambda_1(s, m_f) + a_{\text{V}f}\gamma_\rho\gamma_5\Lambda_2(s, m_f) \right] \end{aligned}$$

$$\begin{aligned}
& + v_{Vf} \frac{2m_f(q-q')_\rho}{s} \Lambda_3(s, m_f) + a_{Vf} \frac{2m_f(q+q')_\rho}{s} \gamma_5 \Lambda_4(s, m_f) \Big], \\
\Gamma^{Pf}(q, q') &= eg_{Pf} \gamma_5 \left[1 + Q_f^2 \frac{\alpha}{4\pi} \Lambda_5(s, m_f) \right], \\
\Gamma^{Sf}(q, q') &= ieg_{Sf} \left[1 + Q_f^2 \frac{\alpha}{4\pi} \Lambda_6(s, m_f) \right], \tag{4.3}
\end{aligned}$$

where the momenta q and q' of the vertex functions Γ correspond to the outgoing fermion and antifermion, respectively, and $s = (q + q')^2$. Note that we have already assumed that the fermion fields are on shell, i.e. we have used $q^2 = q'^2 = m_f^2$ and terms that vanish after contraction with Dirac spinors have been omitted. The virtual corrections to these vertices are parametrized by the functions $\Lambda_i(s, m)$. At the one-loop level these are given by

$$\begin{aligned}
\Lambda_1(s, m) &= -3 [B_0(s, m, m) - B_0(0, m, m) - 2] - 2(s - 2m^2)C_0(m^2, s, m^2, m_\gamma, m, m) \\
&\quad + 4m^2 B'_0(m^2, m_\gamma, m), \\
\Lambda_2(s, m) &= \frac{8m^2}{s - 4m^2} [B_0(s, m, m) - B_0(0, m, m) - 2], \\
\Lambda_3(s, m) &= -\frac{s}{s - 4m^2} [B_0(s, m, m) - B_0(0, m, m) - 2], \\
\Lambda_4(s, m) &= -2 - \frac{3s - 4m^2}{s - 4m^2} [B_0(s, m, m) - B_0(0, m, m) - 2], \\
\Lambda_5(s, m) &= \Lambda_1(s, m) - \Lambda_2(s, m) - \Lambda_4(s, m) \\
&= 2 - 2(s - 2m^2)C_0(m^2, s, m^2, m_\gamma, m, m) + 4m^2 B'_0(m^2, m_\gamma, m), \\
\Lambda_6(s, m) &= 2 - \frac{8m^2}{s - 4m^2} [B_0(s, m, m) - B_0(0, m, m) - 2] \\
&\quad - 2(s - 2m^2)C_0(m^2, s, m^2, m_\gamma, m, m) + 4m^2 B'_0(m^2, m_\gamma, m). \tag{4.4}
\end{aligned}$$

The appearing scalar integrals are easily calculated to

$$\begin{aligned}
B_0(s, m, m) - B_0(0, m, m) - 2 &= \beta_s \ln(x_s), \\
C_0(m^2, s, m^2, m_\gamma, m, m) &= \frac{1}{\beta_s s} \left[\ln\left(\frac{m_\gamma^2}{m^2}\right) \ln(x_s) + \frac{1}{2} \ln^2(x_s) + 2 \text{Li}_2(1 + x_s) \right. \\
&\quad \left. - \frac{\pi^2}{2} - 2\pi i \ln(1 + x_s) \right], \\
B'_0(m^2, m_\gamma, m) &= \frac{\partial B_0}{\partial p^2}(p^2, m_\gamma, m) \Big|_{p^2=m^2} = -\frac{1}{m^2} \left[1 + \ln\left(\frac{m_\gamma}{m}\right) \right], \tag{4.5}
\end{aligned}$$

where

$$\beta_s = \sqrt{1 - \frac{4m^2}{s} + i\epsilon}, \quad x_s = \frac{\beta_s - 1}{\beta_s + 1}, \tag{4.6}$$

and $\text{Li}_2(x)$ denotes the usual dilogarithm. As indicated in Eq. (4.4), not all of the functions Λ_i are independent. Owing to the Ward identity (3.7), the correction to the $\chi f \bar{f}$ vertex, and thus the function Λ_5 , is completely fixed by the correction to the $Z f \bar{f}$ vertex.

When applied to the process (2.1), the parametrization (4.3) can be directly inserted to calculate the final-state corrections, while the corrections to the initial-state vertices follow from obvious substitutions. The complete vertex correction to the amplitude is given by

$$\begin{aligned}
\mathcal{M}_{\text{vert}}^{(\gamma)} = & \frac{\alpha}{4\pi} \sum_{V=\gamma,Z} \left\{ \left[Q_\mu^2 \Lambda_1(s, m_\mu) + Q_f^2 \Lambda_1(s, m_f) \right] \mathcal{M}_{V,0} \right. \\
& + \frac{e^2}{s - \hat{M}_V^2} \left[Q_\mu^2 a_{V\mu} \Lambda_2(s, m_\mu) \left(v_{Vf} \mathcal{M}_1^{av} - a_{Vf} \mathcal{M}_1^{aa} \right) \right. \\
& \quad + Q_f^2 a_{Vf} \Lambda_2(s, m_f) \left(v_{V\mu} \mathcal{M}_1^{va} - a_{V\mu} \mathcal{M}_1^{aa} \right) \\
& \quad + Q_\mu^2 v_{V\mu} \Lambda_3(s, m_\mu) \frac{4m_\mu}{s} \left(v_{Vf} \mathcal{M}_4^{vv} - a_{Vf} \mathcal{M}_4^{va} + m_f a_{Vf} \mathcal{M}_2^{va} \right) \\
& \quad + Q_f^2 v_{Vf} \Lambda_3(s, m_f) \frac{4m_f}{s} \left(v_{V\mu} \mathcal{M}_3^{vv} - a_{V\mu} \mathcal{M}_3^{av} - m_\mu a_{V\mu} \mathcal{M}_2^{av} \right) \\
& \quad \left. \left. + a_{V\mu} a_{Vf} \frac{4m_\mu m_f}{s} \left[Q_\mu^2 \Lambda_4(s, m_\mu) + Q_f^2 \Lambda_4(s, m_f) \right] \mathcal{M}_2^{aa} \right] \right\} \\
& + \frac{\alpha}{4\pi} \sum_{P=\chi,A} \left[Q_\mu^2 \Lambda_5(s, m_\mu) + Q_f^2 \Lambda_5(s, m_f) \right] \mathcal{M}_{P,0} \\
& + \frac{\alpha}{4\pi} \sum_{S=h,H} \left[Q_\mu^2 \Lambda_6(s, m_\mu) + Q_f^2 \Lambda_6(s, m_f) \right] \mathcal{M}_{S,0}, \tag{4.7}
\end{aligned}$$

where we made use of the lowest-order structures $\mathcal{M}_{V,0}$, $\mathcal{M}_{P,0}$, and $\mathcal{M}_{S,0}$ defined in Eq. (2.11).

4.1.2 Box corrections

Compared to the vertex corrections, the calculation of the box diagrams, which are shown in Figure 3, involves quite a lot of algebra. In fact, the full result for the box corrections is too lengthy and involved to be reported here. Instead we give the most important gauge-invariant part of the boxes, denoted by $\mathcal{M}_{\text{box,res}}^{(\gamma)}$, which contains the complete IR structure and all resonant contributions. To this end, we split the box correction according to

$$\mathcal{M}_{\text{box}}^{(\gamma)} = \mathcal{M}_{\text{box,res}}^{(\gamma)} + \mathcal{M}_{\text{box,cont}}^{(\gamma)}. \tag{4.8}$$

The finite remainder $\mathcal{M}_{\text{box,cont}}^{(\gamma)}$, which describes box corrections to the continuum, will not be given analytically, but it is included in the numerical results below.

The part $\mathcal{M}_{\text{box,res}}^{(\gamma)}$ is obtained from the full box diagrams upon setting the integration momentum in the numerator of the diagram to the value that corresponds to zero-momentum transfer by the photon. If two photons are exchanged in the box, there are two such values of the integration momentum, leading to two independent contributions. Obviously, this procedure extracts the complete IR-sensitive part of the box diagrams, as can be shown by simple power counting: if q_γ is the photon momentum, the difference between the full box and the extracted part contains a factor q_γ , which cancels the (logarithmic) IR divergence ($q_\gamma \rightarrow 0$) of the denominator. The integration domain near $q_\gamma \rightarrow 0$ is, however, also the only source of potentially resonant contributions of the box diagrams.

A resonance requires $s \sim M_X^2$, where X denotes any boson exchanged at tree level, and the only way to preserve the condition $q_X^2 \sim s \sim M_X^2$ (q_X denoting the momentum of X) in the box diagram is to require that the photon, which also connects initial and final state, is soft ($q_\gamma \rightarrow 0$). Otherwise the X propagator becomes non resonant. Since we did not set $q_\gamma \rightarrow 0$ in the X propagator denominator in our definition of $\mathcal{M}_{\text{box,res}}^{(\gamma)}$, the full leading resonance behaviour of each box is still contained in this part of the box amplitudes. The actual calculation of $\mathcal{M}_{\text{box,res}}^{(\gamma)}$ is rather simple, since it involves only scalar integrals, and the result is

$$\mathcal{M}_{\text{box,res}}^{(\gamma)} = Q_\mu Q_f \frac{\alpha}{\pi} \sum_{X=\gamma, Z, h, H, X, A} \left[(m_\mu^2 + m_f^2 - t) D_0(t, \hat{M}_X) - (t \leftrightarrow u) \right] \times (s - \hat{M}_X^2) \mathcal{M}_{X,0} / (1 + \delta_{X\gamma}), \quad (4.9)$$

where $\delta_{X\gamma} = 1$ for $X = \gamma$ and $\delta_{X\gamma} = 0$ otherwise. The gauge invariance of this part of the one-loop amplitude simply follows from the gauge invariance of the $Q_\mu Q_f$ part of the IR divergence, which is completely contained in $\mathcal{M}_{\text{box,res}}^{(\gamma)}$. The IR-divergent scalar box integrals D_0 , including the generalization to complex masses \hat{M}_X , have been calculated in Ref. [35]; the results read

$$\begin{aligned} D_0(t, \hat{M}_X) &= D_0(m_\mu^2, m_\mu^2, m_f^2, m_f^2, s, t, m_\gamma, m_\mu, \hat{M}_X, m_f) \\ &= \frac{1}{(s - \hat{M}_X^2) \sqrt{\lambda(t, m_\mu^2, m_f^2)}} \left\{ 2 \ln(x_t) \left[\ln(1 - x_t^2) - \ln\left(\frac{\hat{M}_X m_\gamma}{\hat{M}_X^2 - s}\right) \right] \right. \\ &\quad \left. - \sum_{\rho, \sigma=\pm 1} \left[\text{Li}_2(x_t x_\mu^\rho x_f^\sigma) + \left(\ln(x_t) + \ln(x_\mu^\rho) + \ln(x_f^\sigma) \right) \ln(1 - x_t x_\mu^\rho x_f^\sigma) \right] \right. \\ &\quad \left. + \frac{\pi^2}{2} + \text{Li}_2(x_t^2) + \ln^2(x_\mu) + \ln^2(x_f) \right\} \quad \text{for } X \neq \gamma, \\ D_0(t, \hat{M}_\gamma) &= D_0(m_\mu^2, m_\mu^2, m_f^2, m_f^2, s, t, m_\gamma, m_\mu, m_\gamma, m_f) \\ &= -\frac{1}{s \sqrt{\lambda(t, m_\mu^2, m_f^2)}} 2 \ln(x_t) \ln\left(-\frac{m_\gamma^2}{s} + i\epsilon\right), \end{aligned} \quad (4.10)$$

where we have used the usual definition

$$\lambda(x, y, z) = x^2 + y^2 + z^2 - 2xy - 2xz - 2yz \quad (4.11)$$

and the abbreviations

$$\begin{aligned} x_t &= \frac{\beta_t - 1}{\beta_t + 1}, & \beta_t &= \sqrt{1 - \frac{4m_\mu m_f}{t - (m_\mu - m_f)^2} + i\epsilon}, \\ x_a &= \sqrt{\frac{1 - \beta_{aX}}{1 + \beta_{aX}}}, & \beta_{aX} &= \sqrt{1 - \frac{4m_a^2}{\hat{M}_X^2}}, \quad a = \mu, f, \quad X \neq \gamma. \end{aligned} \quad (4.12)$$

Note that the explicit factor $(s - \hat{M}_X^2)$ in Eq. (4.9) is cancelled by the prefactor in the D_0 functions, but the resonance factor in the lowest-order structure $\mathcal{M}_{X,0}$ survives.

It is instructive to inspect the part $\mathcal{M}_{\text{box,res}}^{(\gamma)}$ from a different point of view. Each contribution from $X \neq \gamma$ can also be viewed as the leading term in an expansion of the corresponding box diagram about the resonance pole. Hence, these terms are nothing but the virtual part of the so-called *non-factorizable* corrections which were discussed in detail in Ref. [37] for several processes with W and Z resonances.⁴ From the results given there it is also clear that the resonant part of $\mathcal{M}_{\text{box,res}}^{(\gamma)}$ will be completely compensated by its counterpart from soft photon emission. Thus, we can expect that the sum of virtual and real initial-final corrections to the resonances will be very small, as it is also known (see e.g. Ref. [18] and references therein) for the Z resonance in e^+e^- collisions for a long time.

Since the continuum contribution $\mathcal{M}_{\text{box,cont}}^{(\gamma)}$ is gauge-invariant and does not involve resonant terms, there is no need to introduce complex masses in this part. Thus, we keep all masses real in the tensor integrals there. Introducing complex masses would change the cross section by terms of $\mathcal{O}(\alpha\Gamma_X/M_X)$ which is beyond the desired level of accuracy.

If one is only interested in resonance cross sections, a simple approximation for the corrections in the vicinity of the resonance at $s \sim M_X^2$ is provided by the neglect of the continuum contribution $\mathcal{M}_{\text{box,cont}}^{(\gamma)}$. This approach is known as *pole approximation* and, for instance, successfully applied for Drell–Yan-like W production at hadron colliders [38] and W-pair production in e^+e^- annihilation [39]. One advantage of this approximation is certainly its simplicity compared to the full off-shell calculation.

4.2 Real photonic corrections

4.2.1 Amplitudes for $\mu^-\mu^+ \rightarrow f\bar{f}\gamma$

The real photonic $\mathcal{O}(\alpha)$ corrections are induced by the process

$$\mu^-(p, \sigma) + \mu^+(p', \sigma') \longrightarrow f(q, \tau) + \bar{f}(q', \tau') + \gamma(k, \lambda) \quad (4.13)$$

in lowest order, where k and λ denote the momenta and helicity of the emitted photon, respectively. Typical diagrams for this process are shown in Figure 4. For the case of the SM the helicity amplitudes have already been given in Ref. [40]. In the following we modify and generalize these amplitudes for our purposes. For completeness we repeat here the basic definitions needed to evaluate the amplitudes, but suppress most of the details concerning their derivation, which was done within the Weyl–van der Waerden (WvdW) spinor technique. We consistently use the variant of the WvdW formalism described in Ref. [40], where also references to other spinor techniques are given.

In the WvdW formalism, each of the momenta p^μ , etc., is written as a complex 2×2 matrix $P_{\dot{A}B}$, etc., consistently denoted by the respective capital letter in the following. These matrices are decomposed into Weyl spinors as follows,

$$P_{\dot{A}B}^{(\iota)} = \sum_{i=1,2} \kappa_{i,\dot{A}}^{(\iota)} \kappa_{i,B}^{(\iota)}, \quad Q_{\dot{A}B}^{(\iota)} = \sum_{i=1,2} \rho_{i,\dot{A}}^{(\iota)} \rho_{i,B}^{(\iota)}, \quad K_{\dot{A}B} = k_{\dot{A}} k_B, \quad (4.14)$$

⁴Actually $\mathcal{M}_{\text{box,res}}^{(\gamma)}$ differs from the non-factorizable corrections by non-resonant contributions, since the off-shellness s is set to its resonance value in the latter.

where a dotted spinor index indicates complex conjugation. Using polar coordinates for the momentum p ,

$$p^\mu = (p_0, |\mathbf{p}| \cos \phi_p \sin \theta_p, |\mathbf{p}| \sin \phi_p \sin \theta_p, |\mathbf{p}| \cos \theta_p), \quad (4.15)$$

the (covariant) spinors $\kappa_{i,A}$ are given by

$$\kappa_{1,A} = \sqrt{p_0 + |\mathbf{p}|} \begin{pmatrix} e^{-i\phi_p} \cos \frac{\theta_p}{2} \\ \sin \frac{\theta_p}{2} \end{pmatrix} \quad \kappa_{2,A} = \sqrt{p_0 - |\mathbf{p}|} \begin{pmatrix} \sin \frac{\theta_p}{2} \\ -e^{+i\phi_p} \cos \frac{\theta_p}{2} \end{pmatrix}. \quad (4.16)$$

Moreover, contravariant spinors are defined according to

$$\phi^A = \epsilon^{AB} \phi_B, \quad \epsilon^{AB} = \begin{pmatrix} 0 & +1 \\ -1 & 0 \end{pmatrix}. \quad (4.17)$$

The application to $\kappa'_{i,A}$ and $\rho_{i,A}^{(\prime)}$ is obvious. The spinor k_A is constructed from the momentum k^μ in the same way as $\kappa_{1,A}$ from p^μ (the counterpart of $\kappa_{2,A}$ vanishes for light-like momenta). For two Weyl spinors ϕ_A and ψ_A the antisymmetric product

$$\langle \phi \psi \rangle = \phi_A \psi^A = \phi_1 \psi_2 - \phi_2 \psi_1, \quad \langle \phi \psi \rangle^* = \phi_{\dot{A}} \psi^{\dot{A}} = (\phi_1 \psi_2 - \phi_2 \psi_1)^*, \quad (4.18)$$

turns out to be very useful, since both Minkowski products and Dirac spinor chains can be written in terms of such products. For helicity eigenstates of fermions, the Dirac spinors can be expressed in terms of the associated momentum spinors in a very simple way. In our case we can write the Dirac spinors as

$$u_{\mu^-} = \begin{pmatrix} \phi_A \\ \psi^{\dot{A}} \end{pmatrix}, \quad \bar{v}_{\mu^+} = (\psi'^A, \phi'_{\dot{A}}), \quad \bar{u}_f = (\eta^A, \xi_{\dot{A}}), \quad v_{\bar{f}} = \begin{pmatrix} \xi'_{\dot{A}} \\ \eta'^A \end{pmatrix}, \quad (4.19)$$

with the actual insertions

$$\begin{aligned} (\phi, \psi) &= \begin{cases} (\kappa_1, -\kappa_2) & \text{for } \sigma = +, \\ (\kappa_2, \kappa_1) & \text{for } \sigma = -, \end{cases} & (\phi', \psi') &= \begin{cases} (\kappa'_1, \kappa'_2) & \text{for } \sigma' = -, \\ (-\kappa'_2, \kappa'_1) & \text{for } \sigma' = +, \end{cases} \\ (\xi, \eta) &= \begin{cases} (\rho_1, -\rho_2) & \text{for } \tau = +, \\ (\rho_2, \rho_1) & \text{for } \tau = -, \end{cases} & (\xi', \eta') &= \begin{cases} (\rho'_1, \rho'_2) & \text{for } \tau' = -, \\ (-\rho'_2, \rho'_1) & \text{for } \tau' = +, \end{cases} \end{aligned} \quad (4.20)$$

for the various polarizations.

The helicity amplitudes \mathcal{M}_γ for the process (4.13) read

$$\mathcal{M}_\gamma(\sigma, \sigma', \tau, \tau', \lambda) = \sqrt{2}e^3 \left[\sum_{V=\gamma, Z} A_\lambda^{(V)}(\sigma, \sigma', \tau, \tau') + \sum_{\varphi=\chi, h, H, A} A_\lambda^{(\varphi)}(\sigma, \sigma', \tau, \tau') \right], \quad (4.21)$$

where the two generic functions $A_\lambda^{(V)}$ and $A_\lambda^{(\varphi)}$ describe spin-1 and spin-0 exchange, respectively. In the SM the sum over φ extends only over H and χ . For $\lambda = +1$ these functions are given by

$$A_+^{(V)}(\sigma, \sigma', \tau, \tau') = \left\{ \frac{Q_\mu \langle k P' P k \rangle}{2(p \cdot k)(p' \cdot k)[(q + q')^2 - \hat{M}_V^2]} - \frac{Q_f \langle k Q' Q k \rangle}{2(q \cdot k)(q' \cdot k)[(p + p')^2 - \hat{M}_V^2]} \right\}$$

$$\begin{aligned}
& \times \left(g_{\bar{\nu}\mu}^+ g_{\bar{\nu}f}^+ \langle \phi' \xi \rangle^* \langle \phi \xi' \rangle + g_{\bar{\nu}\mu}^+ g_{\bar{\nu}f}^- \langle \phi' \eta' \rangle^* \langle \phi \eta \rangle \right. \\
& \quad \left. + g_{\bar{\nu}\mu}^- g_{\bar{\nu}f}^+ \langle \psi \xi \rangle^* \langle \psi' \xi' \rangle + g_{\bar{\nu}\mu}^- g_{\bar{\nu}f}^- \langle \psi \eta' \rangle^* \langle \psi' \eta \rangle \right) \\
& - \frac{Q_\mu}{(q+q')^2 - \hat{M}_V^2} \left[\frac{g_{\bar{\nu}\mu}^+ \langle k \phi' \rangle^*}{(p' \cdot k)} \left(g_{\bar{\nu}f}^+ \langle k \xi \rangle^* \langle \phi \xi' \rangle + g_{\bar{\nu}f}^- \langle k \eta' \rangle^* \langle \phi \eta \rangle \right) \right. \\
& \quad \left. - \frac{g_{\bar{\nu}\mu}^- \langle k \psi \rangle^*}{(p \cdot k)} \left(g_{\bar{\nu}f}^+ \langle k \xi \rangle^* \langle \psi' \xi' \rangle + g_{\bar{\nu}f}^- \langle k \eta' \rangle^* \langle \psi' \eta \rangle \right) \right] \\
& - \frac{Q_f}{(p+p')^2 - \hat{M}_V^2} \left[\frac{g_{\bar{\nu}f}^+ \langle k \xi \rangle^*}{(q \cdot k)} \left(g_{\bar{\nu}\mu}^+ \langle k \phi' \rangle^* \langle \phi \xi' \rangle + g_{\bar{\nu}\mu}^- \langle k \psi \rangle^* \langle \psi' \xi' \rangle \right) \right. \\
& \quad \left. - \frac{g_{\bar{\nu}f}^- \langle k \eta' \rangle^*}{(q' \cdot k)} \left(g_{\bar{\nu}\mu}^+ \langle k \phi' \rangle^* \langle \phi \eta \rangle + g_{\bar{\nu}\mu}^- \langle k \psi \rangle^* \langle \psi' \eta \rangle \right) \right], \\
A_+^{(\varphi)}(\sigma, \sigma', \tau, \tau') = & \left\{ \frac{Q_f \langle k Q' Q k \rangle}{4(q \cdot k)(q' \cdot k)[(p+p')^2 - \hat{M}_\varphi^2]} - \frac{Q_\mu \langle k P' P k \rangle}{4(p \cdot k)(p' \cdot k)[(q+q')^2 - \hat{M}_\varphi^2]} \right\} \\
& \times \left(g_{\varphi\mu}^+ \langle \phi \psi' \rangle + g_{\varphi\mu}^- \langle \phi' \psi \rangle^* \right) \left(g_{\varphi f}^+ \langle \xi' \eta \rangle + g_{\varphi f}^- \langle \xi \eta' \rangle^* \right) \\
& + \frac{Q_\mu g_{\varphi\mu}^- \langle k \phi' \rangle^* \langle k \psi \rangle^*}{(q+q')^2 - \hat{M}_\varphi^2} \left(g_{\varphi f}^+ \langle \xi' \eta \rangle + g_{\varphi f}^- \langle \xi \eta' \rangle^* \right) \left[\frac{1}{2(p \cdot k)} + \frac{1}{2(p' \cdot k)} \right] \\
& - \frac{Q_f g_{\varphi f}^- \langle k \xi \rangle^* \langle k \eta' \rangle^*}{(p+p')^2 - \hat{M}_\varphi^2} \left(g_{\varphi\mu}^+ \langle \phi \psi' \rangle + g_{\varphi\mu}^- \langle \phi' \psi \rangle^* \right) \left[\frac{1}{2(q \cdot k)} + \frac{1}{2(q' \cdot k)} \right].
\end{aligned} \tag{4.22}$$

Here we made consistent use of the chiral couplings introduced in Eq. (2.6), and the dots stand for ordinary products of four-vectors. Moreover, the following abbreviations are used,

$$\langle k P' P k \rangle = \sum_{i,j=1,2} \langle k \kappa_i' \rangle^* \langle \kappa_j \kappa_i' \rangle \langle \kappa_j k \rangle^*, \quad \langle k Q' Q k \rangle = \sum_{i,j=1,2} \langle k \rho_i' \rangle^* \langle \rho_j \rho_i' \rangle \langle \rho_j k \rangle^*. \tag{4.23}$$

The amplitudes for $\lambda = -1$ follow from discrete symmetries. For instance, a parity transformation leads to the relations

$$\mathcal{M}_\gamma(-\sigma, -\sigma', -\tau, -\tau', -\lambda) = \text{sgn}(\sigma\sigma'\tau\tau') \mathcal{M}_\gamma(\sigma, \sigma', \tau, \tau', \lambda)^* \Big|_{(g_{\dots}^\pm)^* \rightarrow g_{\dots}^\mp, \hat{M}_{\dots}^* \rightarrow \hat{M}_{\dots}}, \tag{4.24}$$

and CP implies

$$\mathcal{M}_\gamma(-\sigma', -\sigma, -\tau', -\tau, -\lambda) = -\text{sgn}(\sigma\sigma'\tau\tau') \mathcal{M}_\gamma(\sigma, \sigma', \tau, \tau', \lambda)^* \Big|_{p \leftrightarrow p', q \leftrightarrow q', (g_{\dots}^\pm)^* \rightarrow g_{\dots}^\pm, \hat{M}_{\dots}^* \rightarrow \hat{M}_{\dots}}. \tag{4.25}$$

The substitutions for $(g_{\dots}^\pm)^*$ and \hat{M}_{\dots}^* ensure (in addition to the interchange of g_{\dots}^+ and g_{\dots}^- in the P transformation) that complex couplings and masses are not subject of taking the complex conjugate of the amplitude.

The bremsstrahlung contribution σ_γ to the cross section is obtained from the transition amplitudes \mathcal{M}_γ by the phase-space integration

$$\sigma_\gamma = \frac{1}{2s\beta_\mu} \int d\Phi_\gamma \sum_{\sigma, \sigma', \tau, \tau', \lambda} \frac{1}{4} (1 + 2P_- \sigma)(1 + 2P_+ \sigma') |\mathcal{M}_\gamma(\sigma, \sigma', \tau, \tau', \lambda)|^2, \tag{4.26}$$

where the phase-space integral is defined by

$$\int d\Phi_\gamma = \int \frac{d^3\mathbf{q}}{(2\pi)^3 2q_0} \int \frac{d^3\mathbf{q}'}{(2\pi)^3 2q'_0} \int \frac{d^3\mathbf{k}}{(2\pi)^3 2k_0} (2\pi)^4 \delta(p + p' - q - q' - k). \quad (4.27)$$

4.2.2 Treatment of infrared singularities

The phase-space integral (4.26) of the real photonic corrections diverges in the IR region, i.e. if the photon energy k_0 tends to zero. As done for the virtual corrections, we regularize this IR divergence by an infinitesimal photon mass m_γ , i.e. the integral (4.26) has to be modified appropriately. We have applied two independent methods for this task, known as *phase-space slicing* and *subtraction*.

In the phase-space slicing approach, the soft-photon region $m_\gamma < k_0 < \Delta E$ is excluded from the integral (4.26) by the energy cut ΔE . If ΔE is chosen sufficiently small the photon-emission cross section can be treated in the soft-photon approximation, where it factorizes into the differential lowest-order cross section $d\sigma_0$ and a universal eikonal factor (see, e.g., Ref. [36]). Integration over k in the soft-photon region yields the simple correction factor δ_{soft} to $d\sigma_0$,

$$\delta_{\text{soft}} = \frac{\alpha}{\pi} \left\{ Q_\mu^2 f(\beta_\mu) + Q_f^2 f(\beta_f) + Q_\mu Q_f [g(t) - g(u)] \right\}, \quad (4.28)$$

where the auxiliary functions f and g read

$$\begin{aligned} f(\beta) &= -\ln\left(\frac{4\Delta E^2}{m_\gamma^2}\right) - \frac{1}{\beta} \ln\left(\frac{1-\beta}{1+\beta}\right) + \frac{1+\beta^2}{2\beta} \left[-\ln\left(\frac{4\Delta E^2}{m_\gamma^2}\right) \ln\left(\frac{1-\beta}{1+\beta}\right) \right. \\ &\quad \left. + 2\text{Li}_2\left(\frac{1-\beta}{1+\beta}\right) - \frac{1}{2} \ln^2\left(\frac{1-\beta}{1+\beta}\right) - \frac{\pi^2}{3} + 2\ln\left(\frac{1-\beta}{1+\beta}\right) \ln\left(\frac{2\beta}{1+\beta}\right) \right], \\ g(t) &= \frac{2(m_\mu^2 + m_f^2 - t)}{\sqrt{\lambda(t, m_\mu^2, m_f^2)}} \left[\ln\left(\frac{a_t m_\mu}{m_f}\right) \ln\left(\frac{4\Delta E^2}{m_\gamma^2}\right) + \frac{1}{4} \ln^2\left(\frac{1-\beta_\mu}{1+\beta_\mu}\right) - \frac{1}{4} \ln^2\left(\frac{1-\beta_f}{1+\beta_f}\right) \right. \\ &\quad \left. + \text{Li}_2\left(1 - \frac{1+\beta_\mu}{v_t} a_t\right) + \text{Li}_2\left(1 - \frac{1-\beta_\mu}{v_t} a_t\right) - \text{Li}_2\left(1 - \frac{1+\beta_f}{v_t}\right) \right. \\ &\quad \left. - \text{Li}_2\left(1 - \frac{1-\beta_f}{v_t}\right) \right], \end{aligned} \quad (4.29)$$

with the abbreviations

$$a_t = \frac{m_\mu^2 + m_f^2 - t + \sqrt{\lambda(t, m_\mu^2, m_f^2)}}{2m_\mu^2}, \quad v_t = \frac{2(a_t^2 m_\mu^2 - m_f^2)}{s(a_t - 1)}, \quad (4.30)$$

and the analogous quantities a_u and v_u , obtained from a_t and v_t by $t \rightarrow u$. It can be checked easily that all IR-singular logarithms $\ln m_\gamma$ of δ_{soft} are compensated by their counterparts of the virtual corrections. When adding the parts of σ_γ obtained from the soft and hard regions, the logarithms of the auxiliary cut ΔE cancel in the limit $\Delta E \rightarrow 0$. Note that in the hard regime these logarithms result from a numerical integration. The cancellation proceeds up to terms of $\mathcal{O}(\Delta E/\varepsilon)$, where ε is a typical scale in the process.

Since $\varepsilon \sim \Gamma_\varphi$ is of the order of some MeV in the vicinity of the light Higgs resonances, the cut ΔE has to be chosen extremely small there in order to achieve reasonable accuracy in the phase-space integration of σ_γ .

This numerical subtlety is circumvented in subtraction methods. Here, the general idea is to subtract and to add a simple auxiliary function from the singular integrand. This auxiliary function has to be chosen such that it cancels all singularities of the original integrand so that the phase-space integration of the difference can be performed numerically. Moreover, the auxiliary function has to be simple enough so that it can be integrated over the singular regions analytically, when the subtracted contribution is added again.

We have applied the subtraction method presented in Ref. [41], where the so-called *dipole formalism*, originally introduced by Catani and Seymour [42] within massless QCD, was applied to photon radiation and generalized to massive fermions. Since the actual implementation of this formalism in our calculation does not involve any subtleties, we do not describe it here but refer to Ref. [41] for details. In particular, the application to the process $\mu^- \mu^+ \rightarrow \nu_e \bar{\nu}_e$, which receives the same initial-state corrections as the general $f\bar{f}$ production process (2.1), is spelled out there explicitly.

The numerical results shown below have been obtained using the subtraction approach, since the corresponding Monte Carlo integration errors are considerably smaller than for the slicing method if the same number of integration points is used in either case. We have checked that the results of the two methods agree within the integration errors.

4.2.3 Leading initial-state radiation beyond $\mathcal{O}(\alpha)$

The emission of photons collinear to incoming high-energetic charged fermions, such as e^\pm or μ^\pm with energies of at least several 10 GeV, leads to corrections that are enhanced by large logarithms. These leading logarithms are process independent, and their contribution to the cross section can be obtained by a convolution of the lowest-order cross section with a structure function, which is explicitly known up to $\mathcal{O}(\alpha^3)$ [19, 43]. Following the conventions of Ref. [43], this convolution reads

$$\sigma_{\text{LL}}(s) = \int_0^1 dx \phi(2\alpha, x, Q^2) \sigma_0(xs), \quad (4.31)$$

where $\sigma_0(xs)$ is the lowest-order cross section at the reduced CM energy squared xs . The flux function $\phi(2\alpha, x, Q^2)$ accounts for radiation from both initial-state muons and is connected to the QED splitting function Γ^{LL} , which is up to order $\mathcal{O}(\alpha^3)$ given by

$$\begin{aligned} \Gamma^{\text{LL}}(x, Q^2) &= \phi(\alpha, x, Q^2) \\ &= \frac{\exp\left(-\frac{1}{2}\beta_{\text{ISR}}\gamma_E + \frac{3}{8}\beta_{\text{ISR}}\right) \beta_{\text{ISR}}}{\Gamma\left(1 + \frac{1}{2}\beta_{\text{ISR}}\right)} \frac{\beta_{\text{ISR}}}{2} (1-x)^{\frac{\beta_{\text{ISR}}}{2}-1} - \frac{\beta_{\text{ISR}}}{4} (1+x) \\ &\quad - \frac{\beta_{\text{ISR}}^2}{32} \left\{ \frac{1+3x^2}{1-x} \ln(x) + 4(1+x) \ln(1-x) + 5+x \right\} \\ &\quad - \frac{\beta_{\text{ISR}}^3}{384} \left\{ (1+x) \left[6 \text{Li}_2(x) + 12 \ln^2(1-x) - 3\pi^2 \right] \right. \\ &\quad \left. + \frac{1}{1-x} \left[\frac{3}{2}(1+8x+3x^2) \ln(x) + 6(x+5)(1-x) \ln(1-x) \right] \right\} \end{aligned}$$

$$\begin{aligned}
& + 12(1+x^2)\ln(x)\ln(1-x) - \frac{1}{2}(1+7x^2)\ln^2(x) \\
& + \frac{1}{4}(39-24x-15x^2) \Big] \Big\}, \tag{4.32}
\end{aligned}$$

where β_{ISR} contains the leading logarithm (LL),

$$\beta_{\text{ISR}} = Q_\mu^2 \frac{2\alpha}{\pi} \left(\ln \frac{Q^2}{m_\mu^2} - 1 \right). \tag{4.33}$$

Note that the scale Q^2 is not fixed within LL approximation, but has to be set to a typical scale of the underlying process; for the numerics we use $Q^2 = s$. In Eq. (4.32) γ_E is the Euler constant and $\Gamma(y)$ the gamma function, which should not be confused with the splitting functions. Note that some non-leading terms are incorporated, taking into account the fact that the residue of the soft-photon pole is proportional to $\ln(\dots) - 1$ rather than the logarithm for the initial-state photon radiation.

We add the cross section (4.31) to the one-loop result and subtract the lowest-order and one-loop contributions $\sigma_{\text{LL},1}$ already contained within this formula,

$$\sigma_{\text{LL},1} = \int_0^1 dx \left[\delta(1-x) + 2\Gamma^{\text{LL},1}(x, Q^2) \right] \sigma_0(xs), \tag{4.34}$$

in order to avoid double counting. The one-loop contribution to the structure function reads

$$\begin{aligned}
\Gamma^{\text{LL},1}(x, Q^2) &= \frac{\beta_{\text{ISR}}}{4} \left(\frac{1+x^2}{1-x} \right)_+ \\
&= \frac{\beta_{\text{ISR}}}{4} \lim_{\epsilon \rightarrow 0} \left[\delta(1-x) \left(\frac{3}{2} + 2\ln\epsilon \right) + \theta(1-x-\epsilon) \frac{1+x^2}{1-x} \right]. \tag{4.35}
\end{aligned}$$

In summary, the radiatively corrected cross section σ reads

$$\sigma = \sigma_0 + \sigma_1^{(\gamma)} + \sigma_\gamma + (\sigma_{\text{LL}} - \sigma_{\text{LL},1}), \tag{4.36}$$

where $\sigma_1^{(\gamma)}$ is the virtual photonic one-loop correction. Note that the uncertainty that is connected with the choice of Q^2 enters now in $\mathcal{O}(\alpha^2)$, since all photonic $\mathcal{O}(\alpha)$ corrections, including constant terms, are taken into account.

5 QCD radiative corrections

As already explained in Section 3.2, the diagrams for the $\mathcal{O}(\alpha_s)$ QCD corrections are obtained from the diagrams for the photonic final-state corrections upon replacing the loop-exchanged or emitted photon by a gluon, provided f is a quark. Simple colour algebra shows that the photonic final-state corrections turn into the QCD corrections upon replacing the coupling factor $Q_f^2\alpha$ by $C_F\alpha_s$, where $C_F = 4/3$ is the quadratic Casimir operator of the quark representation. More precisely, this substitution applies to the matrix element $\mathcal{M}_{\text{vert}}^{(\gamma)}$ for the vertex correction in Eq. (4.7), to the squared matrix element $|\mathcal{M}_\gamma|^2$ for hard-photon emission obtained from Eq. (4.21), and to the soft-photon factor

δ_{soft} of Eq. (4.28). The contributions proportional to Q_μ^2 or $Q_\mu Q_f$, of course, have to be set to zero there. We always evaluate the running strong coupling constant $\alpha_s(\mu)$ at the two-loop level including five active flavours in the running, i.e. the top quark is decoupled from the running of $\alpha_s(\mu)$. The renormalization scale is set to $\mu = \sqrt{s}$, which is the total CM energy.

The case that f is a b quark is of particular importance phenomenologically. For this case it is known that the Higgs Yukawa couplings $\varphi b\bar{b}$ receive very large QCD corrections of the form $\alpha_s \ln(m_b/M_H)$ that are connected with the on-shell mass renormalization of the b quark⁵. The convergence of the perturbative series is improved considerably after introducing the $\overline{\text{MS}}$ running b mass $\bar{m}_b(\mu)$ at an appropriate scale μ . To this end, we rescale the $\varphi b\bar{b}$ coupling $g_{\varphi b}$ in all matrix elements according to

$$g_{\varphi b} \rightarrow \bar{g}_{\varphi b}(s) = g_{\varphi b} \times \frac{\bar{m}_b(\sqrt{s})}{m_b}, \quad \varphi = h, H, A, \quad (5.1)$$

which replaces the on-shell mass m_b by the running b mass $\bar{m}_b(\sqrt{s})$ renormalized at the scale $\mu = \sqrt{s}$. Note that $\mu^2 = s$ corresponds to the virtuality of the s -channel Higgs boson φ . The running b mass is evaluated following the results of Ref. [44] (which are also used in *HDECAY*). In order to avoid double counting, the $\mathcal{O}(\alpha_s)$ contribution of the replacement (5.1) has to be subtracted from the one-loop matrix element \mathcal{M}_1 . Using

$$\bar{m}_b(\mu) = m_b \left\{ 1 - \frac{\alpha_s(\mu)}{\pi} \left[\ln \left(\frac{\mu^2}{m_b^2} \right) + \frac{4}{3} \right] + \dots \right\}, \quad (5.2)$$

the consistent modification reads

$$\mathcal{M}_1 \rightarrow \mathcal{M}_1 \Big|_{g_{\varphi b} \rightarrow \bar{g}_{\varphi b}(s)} + \frac{\alpha_s(\sqrt{s})}{\pi} \left[\ln \left(\frac{s}{m_b^2} \right) + \frac{4}{3} \right] \sum_{\varphi=h,H,A} \mathcal{M}_{\varphi,0} \Big|_{g_{\varphi b} \rightarrow \bar{g}_{\varphi b}(s)}. \quad (5.3)$$

Finally, we remark that we have compared our results against the known analytic form of the inclusive next-to-leading order QCD corrections [45] to the on-shell decays of scalar and pseudo-scalar Higgs bosons into heavy quarks. Switching off all non-resonant diagrams in the calculation of the QCD corrections to the resonance cross sections, the relative QCD corrections to the peak cross sections reduce to the corrections to the corresponding partial Higgs decay widths. We find agreement between our numerical results for the relative corrections to the peak cross sections and the corresponding analytical results for the partial Higgs decays within the Monte Carlo integration errors.

6 Numerical results

⁵Actually, analogous logarithms are present in the photonic FSR corrections, but there is no need for a special treatment of those corrections, since they scale with the much smaller factor $Q_f^2 \alpha$ instead of $C_F \alpha_s$.

6.1 Input parameters

For the numerical evaluation we use the following set of SM parameters [46],

$$\begin{aligned}
G_\mu &= 1.16639 \times 10^{-5} \text{ GeV}^{-2}, & \alpha(0) &= 1/137.0359895, \\
\alpha_s(M_Z) &= 0.1181, \\
M_W &= 80.419 \text{ GeV}, & \Gamma_W &= 2.12 \text{ GeV}, \\
M_Z &= 91.1882 \text{ GeV}, & \Gamma_Z &= 2.4952 \text{ GeV}, \\
m_\mu &= 105.658357 \text{ MeV}, & m_\tau &= 1.77703 \text{ GeV}, \\
m_b &= 4.62 \text{ GeV}, & m_t &= 174.3 \text{ GeV}, \\
\bar{m}_s(1 \text{ GeV}) &= 190 \text{ MeV}, & m_c &= 1.42 \text{ GeV}.
\end{aligned} \tag{6.1}$$

Note that part of the input (6.1) is only needed for the calculation of Higgs-boson parameters for which *HDECAY* [22] is used; in particular, this is the case for $\bar{m}_s(1 \text{ GeV})$ which is the $\overline{\text{MS}}$ running strange mass at the renormalization scale 1 GeV.

In order to absorb part of the renormalization effects in the electroweak couplings, such as the running of $\alpha(Q^2)$ from $Q^2 = 0$ to a high-energy scale and some universal effects of the ρ parameter, we derive the electromagnetic coupling $\alpha = e^2/(4\pi)$ from the Fermi constant G_μ according to

$$\alpha_{G_\mu} = \frac{\sqrt{2}G_\mu M_W^2 s_w^2}{\pi}, \tag{6.2}$$

when calculating the couplings for the lowest-order cross sections. In the relative photonic corrections we use $\alpha(0)$ as coupling parameter, which is the correct effective coupling for real photon emission. Thus, the $\mathcal{O}(\alpha)$ -corrected cross section scales like $\alpha(0)\alpha_{G_\mu}^2$. In the following both lowest-order and corrected cross sections for $\mu^- \mu^+ \rightarrow b\bar{b}$ are consistently evaluated with a running b-quark mass, as described in Section 5.

In the MSSM, we take $\tan\beta$ and the mass M_A as the basic input parameters of the Higgs sector. For the evaluation of the Higgs decay widths we need additional input parameters, which are chosen as

$$\begin{aligned}
\mu &= 300 \text{ GeV}, & M_2 &= 200 \text{ GeV}, \\
M_{\tilde{l}_L} &= M_{\tilde{e}_R} = M_{\tilde{q}_L} = M_{\tilde{u}_R} = M_{\tilde{d}_R} = M_{\tilde{L}_L} = M_{\tilde{\tau}_R} = M_{\tilde{Q}_L} = M_{\tilde{t}_R} = M_{\tilde{b}_R} = 1 \text{ TeV}, \\
A_\tau &= A_t = A_b = 1.5 \text{ TeV},
\end{aligned} \tag{6.3}$$

where the notation follows the description of *HDECAY* [22].

Table 1 contains the results, as obtained from *HDECAY*, for the Higgs-boson masses and decay widths, which are used in the following SM and MSSM evaluations.

6.2 The process $\mu^- \mu^+ \rightarrow b\bar{b}$ in the SM

We start our numerical discussion by considering the polarized cross sections for $\mu^- \mu^+ \rightarrow b\bar{b}$ in the SM for $M_H = 115 \text{ GeV}$. The l.h.s. of Figure 6 shows the lowest-order cross sections and their (photonic and QCD) corrected counterparts. We first concentrate on the lowest-order cross sections, where the Higgs-boson resonance occurs only in

SM	$M_{\text{H}}[\text{ GeV}]$	115	150
	$\Gamma_{\text{H}}[\text{ GeV}]$	0.003227	0.01687
MSSM	$\tan\beta$	30	5
	$M_{\text{A}}[\text{ GeV}]$	140	400
	$\Gamma_{\text{A}}[\text{ GeV}]$	2.749	0.7939
	$M_{\text{h}}[\text{ GeV}]$	120.995	115.948
	$\Gamma_{\text{h}}[\text{ GeV}]$	0.1047	0.004083
	$M_{\text{H}}[\text{ GeV}]$	140.658	401.975
	$\Gamma_{\text{H}}[\text{ GeV}]$	2.640	0.4726

Table 1: Higgs-boson masses and decay widths as provided by *HDECAY*

the spin-0 channel, i.e. for μ^\pm with equal helicities, where it appears as a sharp peak at $s = M_{\text{H}}^2$. Apart from the Higgs resonance region, spin-0 contributions to the squared lowest-order matrix element $|\mathcal{M}_0|^2$ are suppressed by a factor $m_\mu^2/M_Z^2 \sim 10^{-6}$ with respect to the spin-1 contributions (μ^\pm with opposite helicities). This suppression factor is clearly visible in the polarized cross sections. At the Higgs resonance an enhancement factor $M_{\text{H}}^2/\Gamma_{\text{H}}^2$ in the squared amplitude $|\mathcal{M}_{\text{H},0}|^2$ compensates this suppression, as long as the total Higgs width does not become too large, which is the case if the Higgs decay into weak gauge bosons is not yet open. In the latter case ($M_{\text{H}} \gtrsim 2M_{\text{W}}$), no Higgs resonance will be visible anymore over the continuous background induced by the spin-1 contribution for realistic degrees of muon beam polarization. Therefore, for the SM we consider $M_{\text{H}} = 115 \text{ GeV}$ and 150 GeV below.

Now we turn to the photonic and QCD corrections to the polarized cross sections, as shown on the l.h.s. of Figure 6. In the spin-1 channels, the cross sections are very similar to its counterpart in e^+e^- annihilation [18], measured at LEP. Above the Z -boson resonance, ISR induces very large positive corrections by the so-called *radiative return* to the Z resonance; these corrections even exceed 100% in relative size. The main difference between muon and e^+e^- collisions is due to the different LL factors β_{ISR} , which are about 0.06 and 0.11 for $Q^2 = M_Z^2$, respectively, i.e. the ISR effects in muon collisions are roughly half as big as in the e^+e^- case. In the spin-0 channels, which contain the Higgs resonance, even much larger positive corrections are visible. These corrections are mainly due to a spin flip of the initial-state muons induced by collinear ISR. Note that this effect is not accounted for by the LL structure-function approach, which is widely used as an approximation for ISR, since this spin-flip correction is not enhanced by a large logarithm. The numerical enhancement is rather due to the extremely large difference between the spin-0 and spin-1 cross sections. Neglecting (irrelevant) corrections that are suppressed by mass factors m_μ^2/s , the spin-flip contribution to the real correction σ_γ takes the universal form [47]

$$\sigma_{\gamma,\text{spin flip}}(P_+, P_-, s) = \frac{\alpha}{2\pi} \int_0^1 dx (1-x) \left[\sigma_0(-P_+, P_-, xs) + \sigma_0(P_+, -P_-, xs) \right], \quad (6.4)$$

which can be deduced from the factorization of collinear photon emission (see e.g. Refs. [41, 48]). Thus, the spin-flip correction $\sigma_{\gamma,\text{spin flip}}(\pm 1, \pm 1, s)$ to the spin-0 chan-

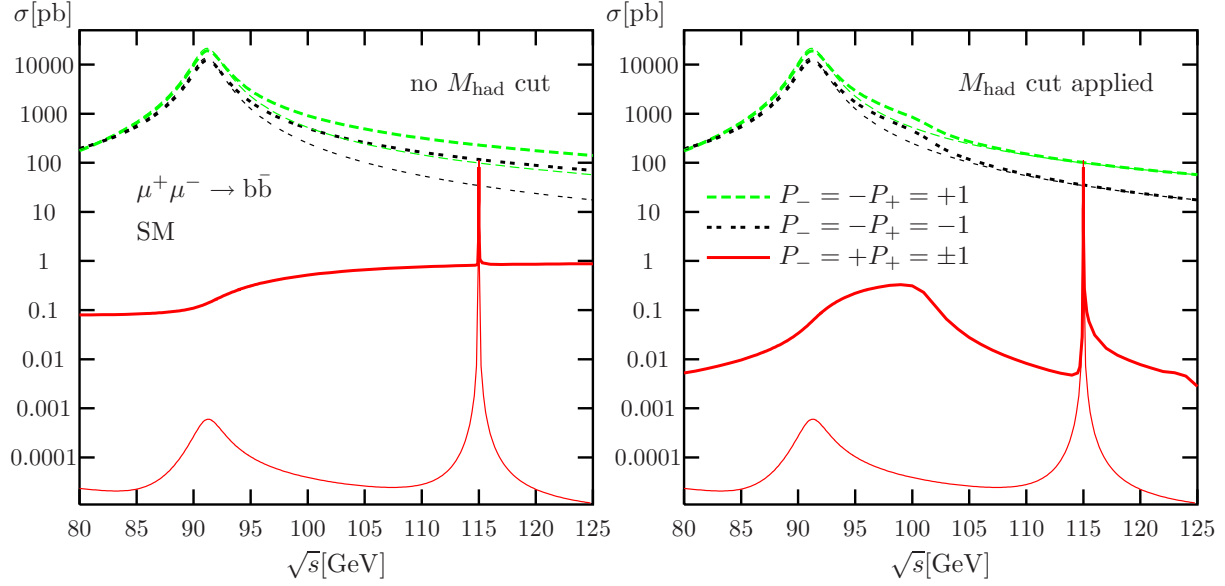


Figure 6: Polarized SM cross sections for $\mu^-\mu^+ \rightarrow b\bar{b}$ in lowest order (thin curves) and including photonic and QCD corrections (thick curves), where no phase-space cuts are applied on the l.h.s. and the invariant-mass cut (6.5) is applied on the r.h.s.

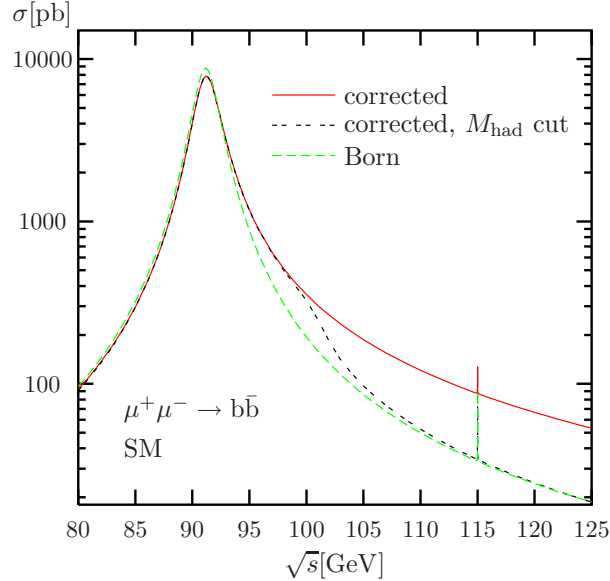


Figure 7: Unpolarized SM cross section for $\mu^-\mu^+ \rightarrow b\bar{b}$ in lowest order and including photonic and QCD corrections, with and without the invariant-mass cut (6.5)

nel receives large contributions from the lowest-order spin-1 cross sections $\sigma_0(\pm 1, \mp 1, xs)$, multiplied by α/π and some numerical factor resulting from the convolution over x . Although these corrections look dramatic for completely polarized beams, they are simply part of the large continuous background to the Higgs resonance that is induced by the spin-1 channel for realistic degrees of beam polarization.⁶

The large ISR corrections from the radiative return can be suppressed by requiring a minimum invariant mass for the $b\bar{b}$ pair that is sufficiently higher than the Z-boson mass. Therefore, we impose the constraint

$$\sqrt{s} - M_{\text{had}} < 10 \text{ GeV} \quad (6.5)$$

in the following, where M_{had} is the invariant mass of all hadrons in the final state, i.e. for gluon emission the gluon momentum is fully included in M_{had} . This cut implies that the energy loss by ISR cannot become larger than 10 GeV. The r.h.s. of Figure 6 shows the lowest-order and corrected polarized cross sections in the presence of this cut. The corrections to the spin-1 channel reduce to moderate size, as expected, but in the spin-0 channels still large corrections remain owing to the spin-flip effect described above.

The effect of the photonic and QCD corrections on the unpolarized cross section for $\mu^- \mu^+ \rightarrow b\bar{b}$ is illustrated in Figure 7 for $M_{\text{H}} = 115 \text{ GeV}$. Apart from the Higgs resonance region, the unpolarized cross section reflects the behaviour of the spin-1 channel discussed above in detail. In the following we restrict our discussion to the case of unpolarized muon beams ($P_{\pm} = 0$), and we always apply the invariant-mass cut (6.5) for $b\bar{b}$ production.

Figures 8 and 9 show close-ups of the Higgs resonances for $M_{\text{H}} = 115 \text{ GeV}$ and $M_{\text{H}} = 150 \text{ GeV}$, respectively. On the l.h.s. the lowest-order predictions for the cross sections are successively improved by including the photonic and QCD corrections. The invariant-mass cut (6.5) implies that the large positive ISR correction of more than 100% turns into a negative correction of $\sim -4\%$ (-8%) off resonance and of $\sim -49\%$ (-46%) for the resonance part for $M_{\text{H}} = 115 \text{ GeV}$ (150 GeV). This leads to a reduction of the resonance peak over the continuous background. The QCD corrections, on the other hand, tend to enhance the resonance peak, since they are positive and larger on resonance than off resonance. For $M_{\text{H}} = 115 \text{ GeV}$ (150 GeV) the resonant part of the cross section is enhanced by $\sim 21\%$ (20%) compared to $\sim 5\%$ (4%) in the continuum. This is in good agreement with the estimate that is based on the neglect of b-mass effects and of interferences between the spin-1 and spin-0 channels. In this approximation the results for the decays $Z, H \rightarrow b\bar{b}$ (see Refs. [18, 45]) can be used deduce the following behaviour of the QCD corrections,

$$\Delta\sigma_{\text{QCD}}(s)\Big|_{m_b \rightarrow 0} \sim \frac{\alpha_s(\sqrt{s})}{\pi} \sigma_{\gamma/Z,0} + \frac{17}{3} \frac{\alpha_s(\sqrt{s})}{\pi} \sigma_{\text{H},0}, \quad (6.6)$$

where $\sigma_{\gamma/Z,0}$ and $\sigma_{\text{H},0}$ denote the contributions to the lowest-order cross section σ_0 induced by γ/Z and Higgs-boson exchange, respectively.

The photonic corrections are dominated by the LL of the ISR corrections in $\mathcal{O}(\alpha)$. The remaining photonic contributions are shown on the r.h.s. of the figures. The largest

⁶The relative weight factor between the spin-1 background and the spin-0 signal cross sections is roughly given by $(1 - P_+ P_-)/(1 + P_+ P_-)$, which will be significantly larger than α/π in practice.

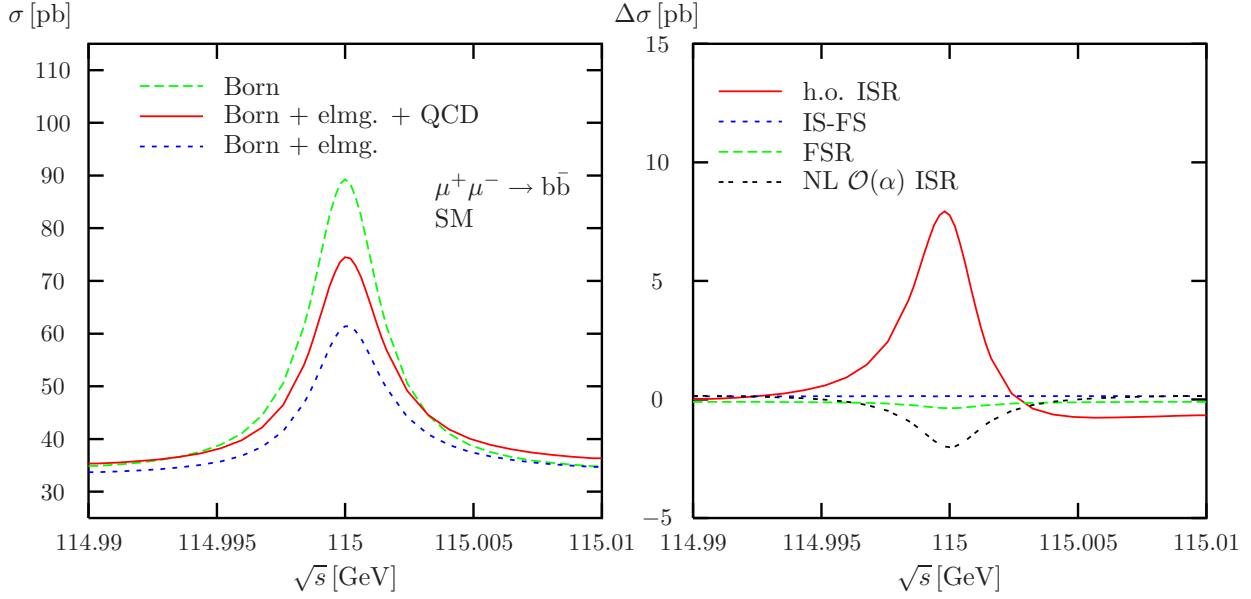


Figure 8: SM cross section $\mu^-\mu^+ \rightarrow b\bar{b}$ near the Higgs resonance for $M_H = 115$ GeV (left) and some contributions to the photonic corrections (right): higher-order ISR (h.o. ISR), initial-final interferences (IS-FS), FSR, and non-leading $\mathcal{O}(\alpha)$ ISR corrections (NL $\mathcal{O}(\alpha)$ ISR)

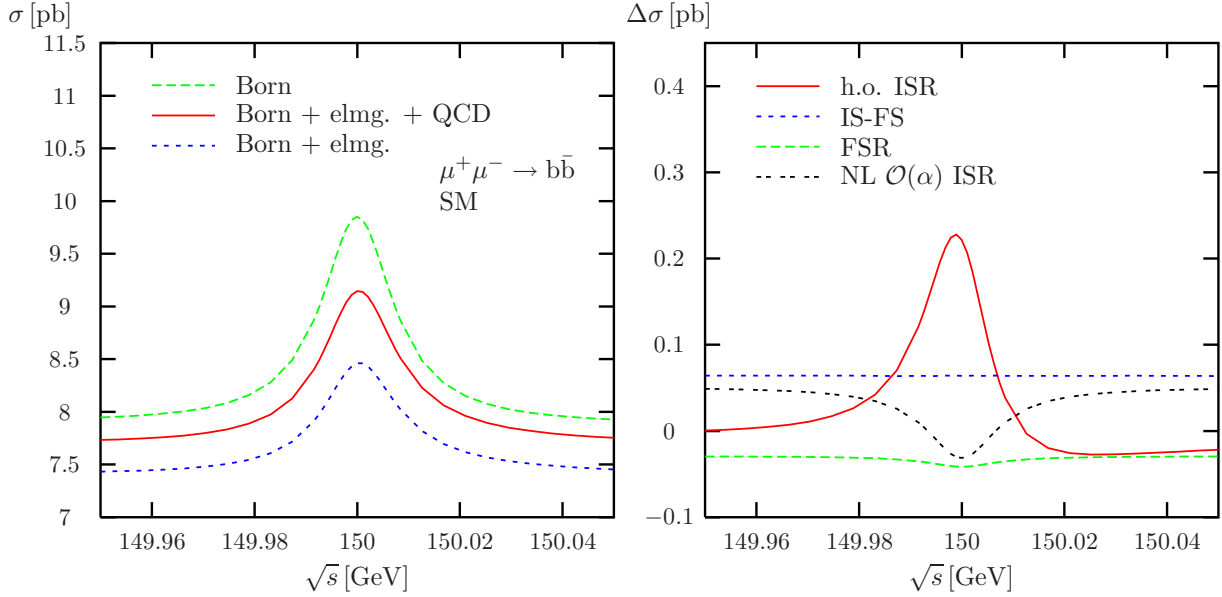


Figure 9: Same as in Figure 8 but for $M_H = 150$ GeV

of these subleading corrections are due to the LL parts beyond $\mathcal{O}(\alpha)$, followed by the non-leading (NL), i.e. non-logarithmic, ISR contributions. Note that the latter are the part of ISR that is not included in the LL approach via the structure function convolution described in Section 4.2.3. The NL $\mathcal{O}(\alpha)$ corrections reduce the peak over background by $\sim 4\%$ for both M_H values. The FSR and initial-final interaction effects turn out to be below 1% of the continuous background and do not show sizable variations in the resonance regions. Thus, they can be safely neglected in all phenomenological investigations of the Higgs resonance.

The Higgs resonances inspected in Figures 8 and 9 are so narrow that the beam energy spread of the muon collider will eventually determine the resonance shape that is seen experimentally. As widely done in the literature, we illustrate this effect by performing a Gaussian convolution of the scattering cross section,

$$\bar{\sigma}(\sqrt{s}) = \frac{1}{\sqrt{2\pi}\delta_{\sqrt{s}}} \int d\sqrt{\hat{s}} \sigma(\sqrt{\hat{s}}) \exp\left\{-\frac{(\sqrt{\hat{s}} - \sqrt{s})^2}{2\delta_{\sqrt{s}}^2}\right\}, \quad (6.7)$$

where \sqrt{s} is the central value of the CM energy and $\delta_{\sqrt{s}}$ the corresponding root-mean-square Gaussian spread. Following Ref. [12] we use

$$\delta_{\sqrt{s}} = 2 \text{ MeV} \left(\frac{R}{0.003\%}\right) \left(\frac{\sqrt{s}}{100 \text{ GeV}}\right) \quad (6.8)$$

with the actual value $R = 0.003\%$. The results of applying this convolution to the resonances shown in Figures 8 and 9 are shown in Figures 10 and 11. As expected, the effect of smearing the resonance is much more pronounced for $M_H = 115 \text{ GeV}$, where the ratio $\delta_{\sqrt{s}}/\Gamma_H$ is ~ 0.7 , than for $M_H = 150 \text{ GeV}$, where the ratio is ~ 0.2 . In both cases, however, the relative impact of the various radiative corrections remains practically unchanged by the smearing.

6.3 The processes $\mu^-\mu^+ \rightarrow b\bar{b}, t\bar{t}$ in the MSSM

Now we turn to Higgs production in the MSSM. Of course, it is beyond the scope of this paper to give an exhaustive overview over the phenomenology of the full supersymmetric parameter space. We rather concentrate on the two MSSM parameter choices given in Table 1, which have been selected to be still experimentally allowed and to cover the most interesting patterns of Higgs resonances: For $\tan\beta = 30$ and $M_A = 140 \text{ GeV}$, the lightest Higgs boson h has a mass of $M_h \sim 121 \text{ GeV}$ with an intermediate width of $\Gamma_h \sim 0.1 \text{ GeV}$, while the resonances of A and H practically lie on top of each other at $M_H \sim M_A = 140 \text{ GeV}$ with large widths $\Gamma_H \sim \Gamma_A \sim 3 \text{ GeV}$. On the other hand, for $\tan\beta = 5$ and $M_A = 400 \text{ GeV}$, the h boson is SM-like with a mass of $M_h \sim 116 \text{ GeV}$ and a narrow width of $\Gamma_h \sim 4 \text{ MeV}$; the A and H resonances in this case are close to each other but separated, since the mass difference $M_H - M_A \sim 2 \text{ GeV}$ is sufficiently larger than the widths $\Gamma_H \sim 0.5 \text{ GeV}$ and $\Gamma_A \sim 0.8 \text{ GeV}$. Note also that in the latter scenario the heavy Higgs bosons can decay into $t\bar{t}$ pairs. Since we do not consider the SM-like h boson any further, the widths of all resonances discussed in the following are much larger than the achievable beam energy spread of a muon collider. Therefore, the smearing hardly affects the resonance shapes shown below, and we can omit the convolution (6.7) in this section.

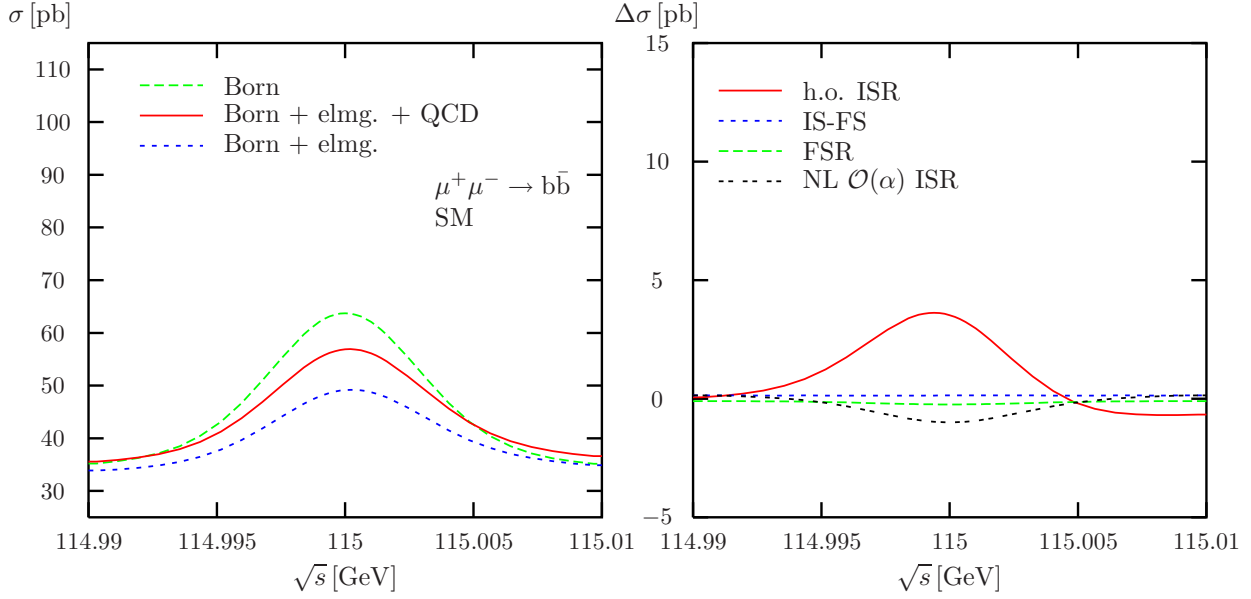


Figure 10: SM cross section $\mu^-\mu^+ \rightarrow b\bar{b}$ near the Higgs resonance for $M_H = 115$ GeV (left) and some contributions to the photonic corrections (right), as in Figure 8, but now with beam energy smearing

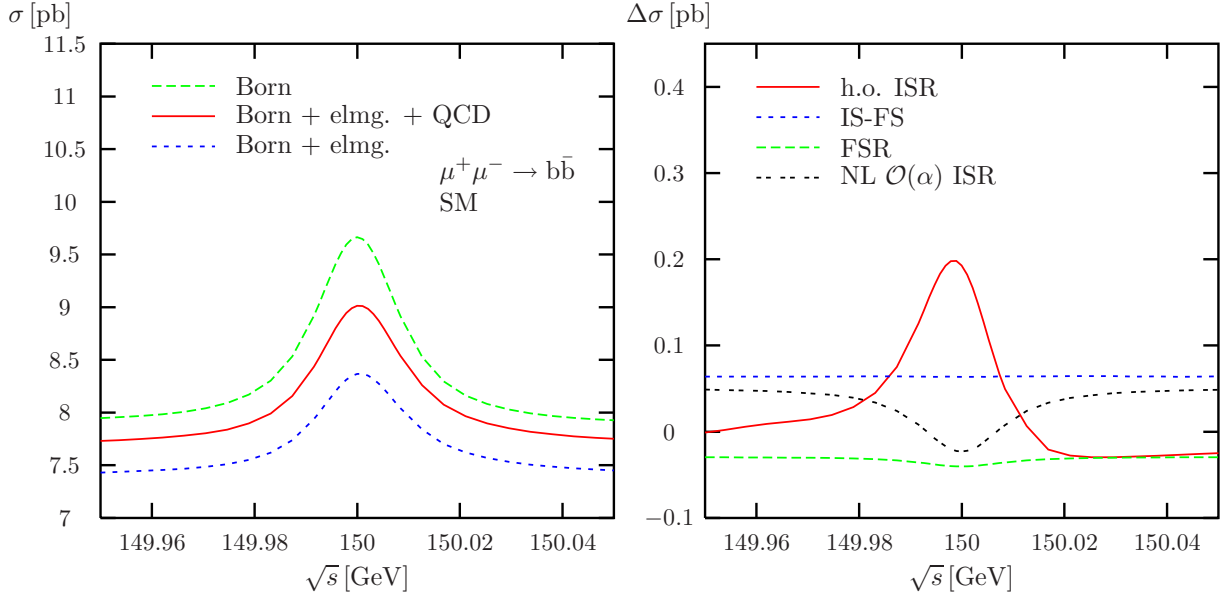


Figure 11: Same as in Figure 10 but for $M_H = 150$ GeV

We first consider the scenario $\tan\beta = 30$ and $M_A = 140$ GeV in Figures 12 and 13, where the h and A/H resonances are shown together with the various radiative corrections, in analogy to the previous section for the SM Higgs boson. The photonic corrections are dominated by the leading ISR logarithms, and the QCD corrections follow the qualitative behaviour of the massless approximation (6.6), where $\sigma_{H,0}$ is replaced by $\sigma_{h/H/A,0}$. Qualitatively the corrections are very similar to the SM case, as expected. The ISR beyond $\mathcal{O}(\alpha)$ tends to enhance the h and A/H resonances by $\sim 7\%$ and $\sim 2\%$, respectively, but the NL ISR tends to reduce the resonances by $\sim 4\%$. Photonic FSR corrections stay below 1% everywhere, and initial-final interferences do not show a resonance behaviour at all.

Of course, the corrections to the SM-like h-boson resonance of the second scenario ($\tan\beta = 5$, $M_A = 400$ GeV) also do not possess any new feature. Therefore, this resonance is not shown explicitly here. More interestingly, Figures 14 and 15 illustrate the A and H resonances, which are close together, for the two processes $\mu^+\mu^- \rightarrow b\bar{b}, t\bar{t}$. We note that we do not apply any cut like (6.5) in the case of $t\bar{t}$ production, i.e. the total cross section is considered, since a radiative return to the Z resonance via ISR is not possible in this channel. For each of the resonances in $b\bar{b}$ production the structure of the corrections again looks as in the previous cases, i.e. the QCD corrections follow the pattern of Eq. (6.6) and the photonic corrections are dominated by the ISR logarithms. The higher-order ISR modifies the resonance cross section by $\sim 8\%$, NL ISR by $\sim -4\%$, FSR by less than 1%, and initial-final interferences not at all. For $t\bar{t}$ production only minor differences are observed. The main difference is the failure of the approximation (6.6), which is due to the large mass of the top quark. The leading ISR effects still dominate the photonic corrections, while higher-order and NL ISR amount to $\sim 6\%$ and $\sim -5\%$ on resonance, respectively. Owing to the omission of an invariant-mass cut on the $t\bar{t}$ system, FSR now becomes positive, but nevertheless does not exceed $\sim 1\%$, in spite of an enhancement by a factor 4 w.r.t. $b\bar{b}$ production induced by the quark charges. Finally, initial-final interferences again do not affect the resonance shape.

7 Conclusions

Muon colliders provide a unique framework for studying Higgs-boson resonances, and thus for measuring Higgs masses, widths, and various couplings. To this end, it is necessary to understand the resonance shapes to high precision, i.e. in particular radiative corrections have to be controlled. In this paper the photonic and QCD radiative corrections to $\mu^+\mu^- \rightarrow f\bar{f}$ have been discussed in detail, both for the SM and the MSSM. In the calculation the issue of a gauge-invariant description of the resonances is emphasized, and the corrections that are relevant for the resonance shape are presented in analytical form.

The most important photonic corrections are due to ISR and amount to $\mathcal{O}(100\%)$. Suppressing the radiative return to the Z-boson resonance by appropriate invariant-mass cuts, the calculated ISR corrections, which include the full $\mathcal{O}(\alpha)$ contributions and leading logarithmic effects up to $\mathcal{O}(\alpha^3)$, should be sufficient to describe photonic corrections within per-cent accuracy. Corrections due to photonic FSR modify the resonance by about 1% or less. Initial-final interferences (box corrections) turn out to be even smaller and non-

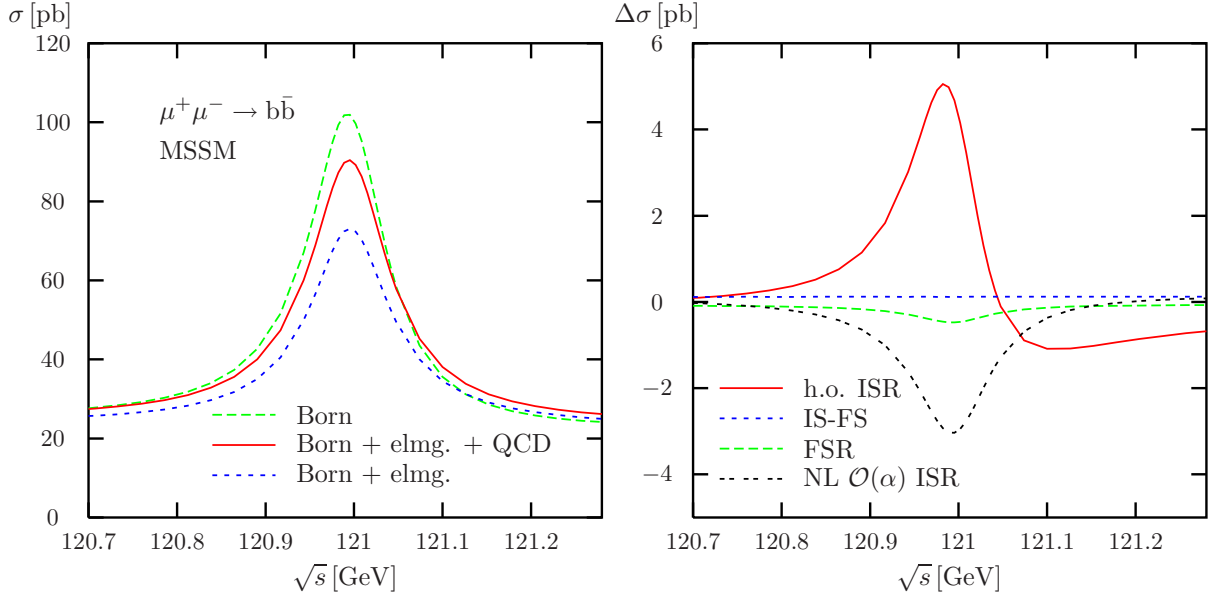


Figure 12: MSSM cross section $\mu^-\mu^+ \rightarrow b\bar{b}$ near the h resonance for $M_A = 140$ GeV and $\tan\beta = 30$ (left) and some contributions to the photonic corrections (right)

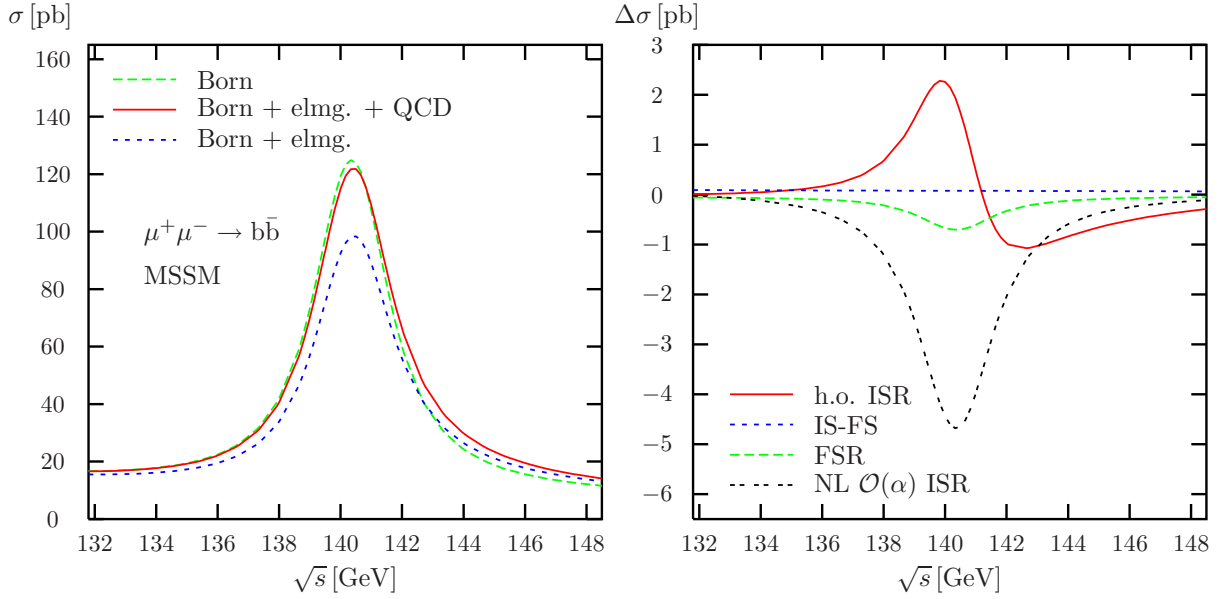


Figure 13: MSSM cross section $\mu^-\mu^+ \rightarrow b\bar{b}$ near the H and A resonances (which lie on top of each other) for $M_A = 140$ GeV and $\tan\beta = 30$ (left) and some contributions to the photonic corrections (right)

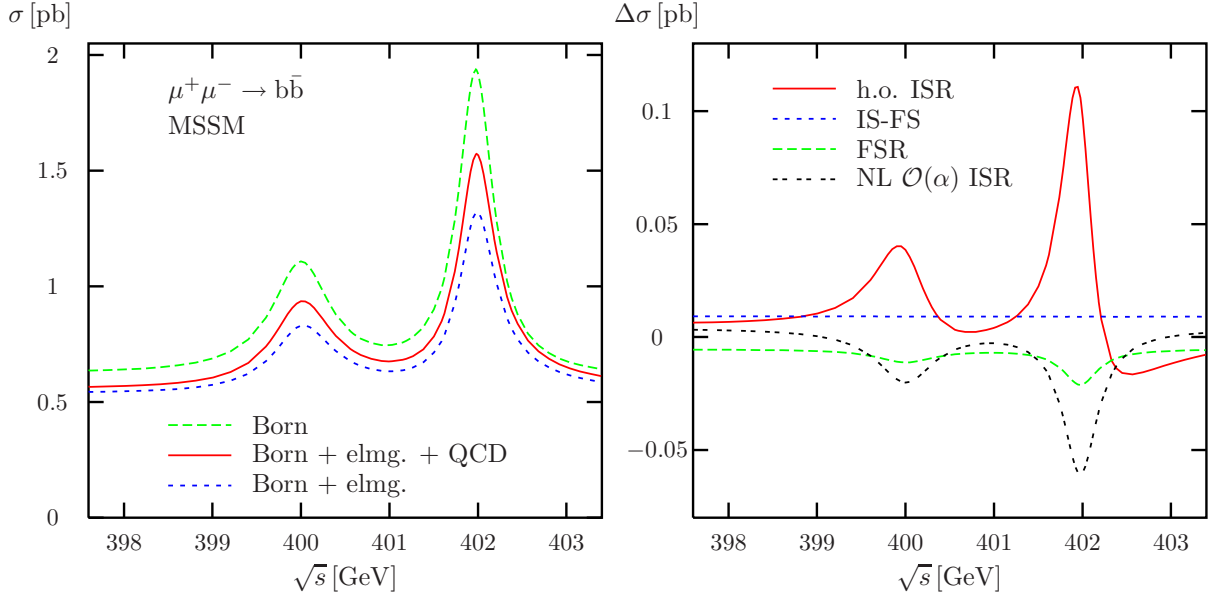


Figure 14: MSSM cross section $\mu^-\mu^+ \rightarrow b\bar{b}$ near the H and A resonances for $M_A = 400$ GeV and $\tan\beta = 5$ (left) and some contributions to the photonic corrections (right)

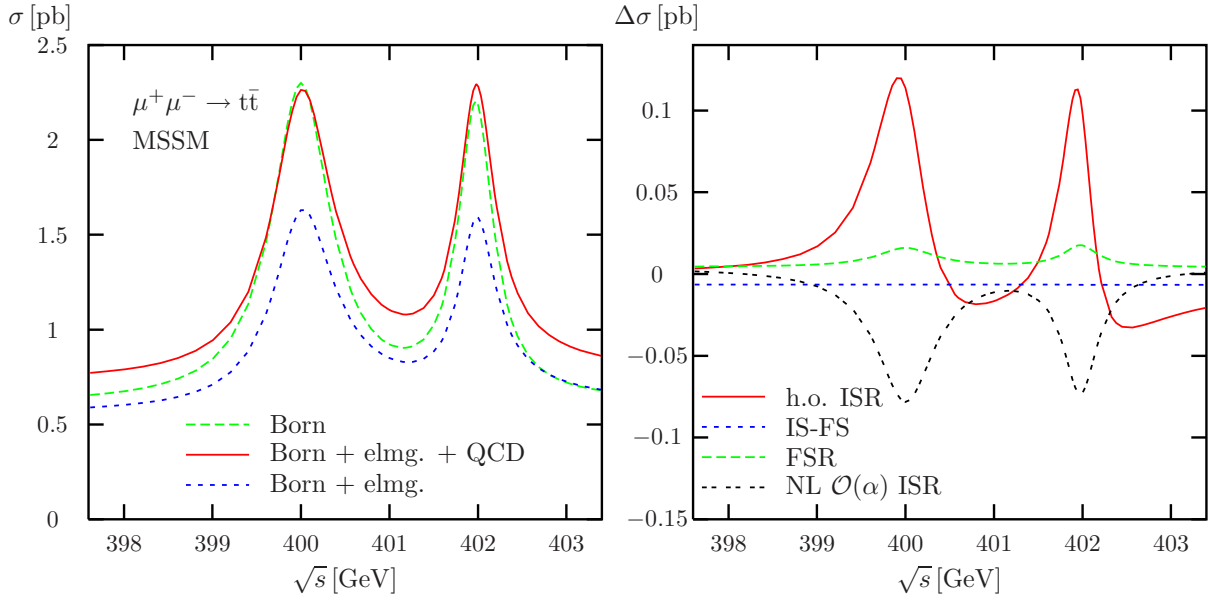


Figure 15: MSSM cross section $\mu^-\mu^+ \rightarrow t\bar{t}$ near the H and A resonances for $M_A = 400$ GeV and $\tan\beta = 5$ (left) and some contributions to the photonic corrections (right)

resonant, i.e. they modify only the continuous background of the resonance. In summary, photonic corrections are now under control at the per-cent level.

QCD corrections have been calculated to $\mathcal{O}(\alpha_s)$ including the full mass dependence. Further improvements beyond $\mathcal{O}(\alpha_s)$ are certainly needed in the future.

The genuine weak corrections are not calculated in this paper. A consistent inclusion of these corrections to the full process $\mu^+\mu^- \rightarrow f\bar{f}$ (keeping all fermion masses non-zero) requires a gauge-invariant Dyson summation of all self-energies, as discussed in some detail. However, for a theoretical description of the Higgs resonances only, the relevant weak corrections can certainly be incorporated in terms of effective couplings, simplifying the task considerably.

Acknowledgements

We thank A. Denner, M. Spira and P.M. Zerwas for valuable discussions and for carefully reading the manuscript.

Appendix

Standard matrix elements

In this appendix we give explicit analytical expressions for the SME introduced in Eq. (2.8) of Section 2, using again the WvdW technique of Ref. [40] as in Section 4.2.1 for the bremsstrahlung matrix elements. Inserting the expressions (4.19) for the Dirac spinors into Eq. (2.8), the SME in terms of WvdW spinor products read

$$\begin{aligned}
\mathcal{M}_1^{xy} &= 2\left(\langle\phi'\xi\rangle^*\langle\phi\xi'\rangle + \delta_x\langle\psi\xi\rangle^*\langle\psi'\xi'\rangle + \delta_y\langle\phi'\eta'\rangle^*\langle\phi\eta\rangle + \delta_x\delta_y\langle\psi\eta'\rangle^*\langle\psi'\eta\rangle\right), \\
\mathcal{M}_2^{xy} &= \left(\langle\phi\psi'\rangle + \delta_x\langle\phi'\psi\rangle^*\right)\left(\langle\xi'\eta\rangle + \delta_y\langle\xi\eta'\rangle^*\right), \\
\mathcal{M}_3^{xy} &= \left(\langle\phi'Q\phi\rangle + \delta_x\langle\psi Q\psi'\rangle\right)\left(\langle\xi'\eta\rangle + \delta_y\langle\xi\eta'\rangle^*\right), \\
\mathcal{M}_4^{xy} &= \left(\langle\phi\psi'\rangle + \delta_x\langle\phi'\psi\rangle^*\right)\left(\langle\xi P\xi'\rangle + \delta_y\langle\eta'P\eta\rangle\right),
\end{aligned} \tag{A.1}$$

where x, y are the vector and axial-vector labels v, a with the sign factors

$$\delta_v = +1, \quad \delta_a = -1. \tag{A.2}$$

Moreover, we have used the shorthands

$$\begin{aligned}
\langle\phi'Q\phi\rangle &= \sum_{i=1,2} \langle\phi'\rho_i\rangle^*\langle\phi\rho_i\rangle, & \langle\psi Q\psi'\rangle &= \sum_{i=1,2} \langle\psi\rho_i\rangle^*\langle\psi'\rho_i\rangle, \\
\langle\eta'P\eta\rangle &= \sum_{i=1,2} \langle\eta'\kappa_i\rangle^*\langle\eta\kappa_i\rangle, & \langle\xi P\xi'\rangle &= \sum_{i=1,2} \langle\xi\kappa_i\rangle^*\langle\xi'\kappa_i\rangle.
\end{aligned} \tag{A.3}$$

The explicit expressions for the various helicity configurations are easily obtained by identifying the generic spinors ϕ, ψ , etc., with the appropriate insertions according to Eq. (4.20).

References

- [1] M. Carena, J. S. Conway, H. E. Haber and J. D. Hobbs *et al.*, arXiv:hep-ph/0010338.
- [2] ATLAS Collaboration, Technical Design Report, CERN–LHCC 99–14 (May 1999); CMS Collaboration, Technical Proposal, CERN–LHCC 94–38 (Dec. 1994).
- [3] E. Accomando *et al.* [ECFA/DESY LC Physics Working Group Collaboration], Phys. Rept. **299** (1998) 1 [arXiv:hep-ph/9705442]; J. A. Aguilar-Saavedra *et al.*, “TESLA Technical Design Report Part III: Physics at an e^+e^- Linear Collider”, arXiv:hep-ph/0106315.
- [4] The LEP Collaborations, the LEP Electroweak Working Group and the SLD Heavy Flavour and Electroweak Groups, arXiv:hep-ex/0112021.
- [5] The LEP Higgs Working Group and the LEP Collaborations, arXiv:hep-ex/0107029.
- [6] The LEP Higgs Working Group and the LEP Collaborations, arXiv:hep-ex/0107030.
- [7] M. Carena, M. Quiros and C. E. Wagner, Nucl. Phys. B **461** (1996) 407 [arXiv:hep-ph/9508343]; H. E. Haber, R. Hempfling and A. H. Hoang, Z. Phys. C **75** (1997) 539 [arXiv:hep-ph/9609331]; S. Heinemeyer, W. Hollik and G. Weiglein, Phys. Rev. D **58** (1998) 091701 [arXiv:hep-ph/9803277].
- [8] M. Carena, H. E. Haber, S. Heinemeyer, W. Hollik, C. E. Wagner and G. Weiglein, Nucl. Phys. B **580** (2000) 29 [arXiv:hep-ph/0001002].
- [9] R. Raja and A. Tollestrup, Phys. Rev. D **58** (1998) 013005 [arXiv:hep-ex/9801004]; C. M. Ankenbrandt *et al.*, Phys. Rev. ST Accel. Beams **2** (1999) 081001 [arXiv:physics/9901022]; W. J. Murray, arXiv:hep-ph/0104268.
- [10] V. D. Barger, M. S. Berger, J. F. Gunion and T. Han, Phys. Rev. Lett. **75** (1995) 1462 [arXiv:hep-ph/9504330].
- [11] V. D. Barger, M. S. Berger, J. F. Gunion and T. Han, Phys. Rept. **286** (1997) 1 [arXiv:hep-ph/9602415].
- [12] V. D. Barger, M. Berger, J. F. Gunion and T. Han, in *Proc. of the APS/DPF/DPB Summer Study on the Future of Particle Physics (Snowmass 2001)* ed. R. Davidson and C. Quigg, arXiv:hep-ph/0110340.
- [13] M. S. Berger, Phys. Rev. Lett. **87** (2001) 131801 [arXiv:hep-ph/0105128].
- [14] B. Grzadkowski and J. F. Gunion, Phys. Lett. B **350** (1995) 218 [arXiv:hep-ph/9501339]; D. Atwood and A. Soni, Phys. Rev. D **52** (1995) 6271 [arXiv:hep-ph/9505233]; S. Y. Choi and J. S. Lee, Phys. Rev. D **61** (2000) 111702 [arXiv:hep-ph/9909315];

- B. Grzadkowski, J. F. Gunion and J. Pliszka, Nucl. Phys. B **583** (2000) 49 [arXiv:hep-ph/0003091];
 E. Asakawa, S. Y. Choi and J. S. Lee, Phys. Rev. D **63** (2001) 015012 [arXiv:hep-ph/0005118].
- [15] V. D. Barger, T. Han and C. G. Zhou, Phys. Lett. B **480** (2000) 140 [arXiv:hep-ph/0002042].
- [16] D. Atwood, L. Reina and A. Soni, Phys. Rev. Lett. **75** (1995) 3800 [arXiv:hep-ph/9507416].
- [17] B. Autin *et al.*, CERN-99-02, ECFA 99-197;
 C. Blöching *et al.*, arXiv:hep-ph/0202199.
- [18] *Z Physics at LEP1*, eds. G. Altarelli, R. Kleiss and C. Verzegnassi (CERN 89-08, Geneva, 1989), Vol. 1.
- [19] E. A. Kuraev and V. S. Fadin, *Yad. Fiz.* **41** (1985) 753 [*Sov. J. Nucl. Phys.* **41** (1985) 466];
 G. Altarelli and G. Martinelli, in “*Physics at LEP*”, eds. J. Ellis and R. Peccei, CERN 86-02 (CERN, Geneva, 1986), Vol. 1, p. 47;
 O. Nicrosini and L. Trentadue, Phys. Lett. B **196** (1987) 551; Z. Phys. C **39** (1988) 479;
 F. A. Berends, W. L. van Neerven and G. J. Burgers, Nucl. Phys. B **297** (1988) 429; Erratum-ibid. B **304** (1988) 921.
- [20] D. M. Pierce, J. A. Bagger, K. T. Matchev and R. J. Zhang, Nucl. Phys. B **491** (1997) 3 [arXiv:hep-ph/9606211];
 M. Carena, D. Garcia, U. Nierste and C. E. Wagner, Nucl. Phys. B **577** (2000) 88 [arXiv:hep-ph/9912516].
- [21] J. F. Gunion and H. E. Haber, Nucl. Phys. B **272** (1986) 1 [Erratum-ibid. B **402** (1986) 567] and *ibid.* B **278** (1986) 449;
 J. F. Gunion, H. E. Haber, G. L. Kane and S. Dawson, *The Higgs Hunters Guide*, Addison-Wesley 1990.
- [22] A. Djouadi, J. Kalinowski and M. Spira, Comput. Phys. Commun. **108** (1998) 56 [arXiv:hep-ph/9704448].
- [23] P. Gambino and P. A. Grassi, Phys. Rev. D **62** (2000) 076002 [arXiv:hep-ph/9907254];
 P. A. Grassi, B. A. Kniehl and A. Sirlin, arXiv:hep-ph/0109228.
- [24] D. Y. Bardin, A. Leike, T. Riemann and M. Sachwitz, Phys. Lett. B **206** (1988) 539;
 D. Wackeroth and W. Hollik, Phys. Rev. D **55** (1997) 6788 [arXiv:hep-ph/9606398];
 W. Beenakker *et al.*, Nucl. Phys. B **500** (1997) 255 [arXiv:hep-ph/9612260].
- [25] M. S. Chanowitz and M. K. Gaillard, Nucl. Phys. B **261** (1985) 379;
 G. J. Gounaris, R. Kögerler and H. Neufeld, Phys. Rev. D **34** (1986) 3257.

- [26] A. Denner and S. Dittmaier, Phys. Rev. D **54** (1996) 4499 [arXiv:hep-ph/9603341].
- [27] A. Denner, S. Dittmaier and G. Weiglein, Nucl. Phys. B **440** (1995) 95 [arXiv:hep-ph/9410338];
X. Y. Li and Y. Liao, Phys. Lett. B **356** (1995) 68.
- [28] R. G. Stuart, Phys. Lett. B **262** (1991) 113;
H. Veltman, Z. Phys. C **62** (1994) 35.
- [29] A. Denner, S. Dittmaier and T. Hahn, Phys. Rev. D **56** (1997) 117 [arXiv:hep-ph/9612390].
- [30] A. Denner, S. Dittmaier, M. Roth and D. Wackerroth, Nucl. Phys. B **560** (1999) 33 [arXiv:hep-ph/9904472].
- [31] J. Küblbeck, M. Böhm and A. Denner, Comput. Phys. Commun. **60** (1990) 165;
H. Eck and J. Küblbeck, *Guide to FeynArts 1.0*, University of Würzburg, 1992.
- [32] R. Mertig, M. Böhm and A. Denner, Comput. Phys. Commun. **64** (1991) 345;
R. Mertig, *Guide to FeynCalc 1.0*, University of Würzburg, 1992.
- [33] G. Passarino and M. Veltman, Nucl. Phys. B **160** (1979) 151.
- [34] G. 't Hooft and M. Veltman, Nucl. Phys. B **153** (1979) 365.
- [35] W. Beenakker and A. Denner, Nucl. Phys. B **338** (1990) 349.
- [36] A. Denner, Fortsch. Phys. **41** (1993) 307.
- [37] K. Melnikov and O. I. Yakovlev, Nucl. Phys. B **471** (1996) 90 [arXiv:hep-ph/9501358];
W. Beenakker, A. P. Chapovsky and F. A. Berends, Nucl. Phys. B **508** (1997) 17 [arXiv:hep-ph/9707326];
A. Denner, S. Dittmaier and M. Roth, Nucl. Phys. B **519** (1998) 39 [arXiv:hep-ph/9710521].
- [38] D. Wackerroth and W. Hollik, Phys. Rev. D **55** (1997) 6788 [arXiv:hep-ph/9606398];
U. Baur, S. Keller and D. Wackerroth, Phys. Rev. D **59** (1999) 013002 [arXiv:hep-ph/9807417];
S. Dittmaier and M. Krämer, arXiv:hep-ph/0109062, to appear in Phys. Rev. D.
- [39] S. Jadach, W. Placzek, M. Skrzypek, B. F. Ward and Z. Was, Phys. Lett. B **417** (1998) 326 [arXiv:hep-ph/9705429];
W. Beenakker, F. A. Berends and A. P. Chapovsky, Nucl. Phys. B **548** (1999) 3 [arXiv:hep-ph/9811481];
A. Denner, S. Dittmaier, M. Roth and D. Wackerroth, Nucl. Phys. B **587** (2000) 67 [arXiv:hep-ph/0006307].
- [40] S. Dittmaier, Phys. Rev. D **59** (1999) 016007 [arXiv:hep-ph/9805445].
- [41] S. Dittmaier, Nucl. Phys. B **565** (2000) 69 [arXiv:hep-ph/9904440].

- [42] S. Catani and M. H. Seymour, Phys. Lett. B **378** (1996) 287 [arXiv:hep-ph/9602277] and Nucl. Phys. B **485** (1997) 291 [Erratum-ibid. B **510** (1997) 291] [arXiv:hep-ph/9605323].
- [43] W. Beenakker *et al.*, in *Physics at LEP2*, eds. G. Altarelli, T. Sjöstrand and F. Zwirner (CERN 96-01, Geneva, 1996), Vol. 1, p. 79 [arXiv:hep-ph/9602351].
- [44] K. G. Chetyrkin, Phys. Lett. B **404** (1997) 161 [arXiv:hep-ph/9703278];
J. A. Vermaseren, S. A. Larin and T. van Ritbergen, Phys. Lett. B **405** (1997) 327 [arXiv:hep-ph/9703284].
- [45] E. Braaten and J. P. Leveille, Phys. Rev. D **22** (1980) 715;
M. Drees and K. i. Hikasa, Phys. Rev. D **41** (1990) 1547.
- [46] D. E. Groom *et al.* [Particle Data Group Collaboration], Eur. Phys. J. C **15** (2000) 1.
- [47] M. Böhm and S. Dittmaier, Nucl. Phys. B **409** (1993) 3;
B. Falk and L. M. Sehgal, Phys. Lett. B **325** (1994) 509.
- [48] R. Kleiss, Z. Phys. C **33** (1987) 433.